Heat fluxes across the Antarctic Circumpolar Current in Drake Passage: Mean flow and eddy contributions

Ramiro Ferrari, Christine Provost, Young-Hyang Park, Nathalie Sennéchael, Zoé Koenig, Hela Sekma, Gilles Garric, Romain Bourdallé-Badie

AGU PUBLICATIONS

JGR

Journal of Geophysical Research: Oceans

RESEARCH ARTICLE

10.1002/2014JC010201

Heat fluxes across the Antarctic Circumpolar Current in Drake Passage: Mean flow and eddy contributions

Ramiro Ferrari[1], Christine Provost[1], Young-Hyang Park[1], Nathalie Sennéchael[1], Zoé Koenig[1], Hela Sekma[1,2], Gilles Garric[3], and Romain Bourdallé-Badie[3]

[1]LOCEAN, UMR 7159, CNRS/UPMC/MNHN/IRD, Université Pierre et Marie Curie, Paris cedex, France, [2]Now at LEGOS, Toulouse, France, [3]MERCATOR-OCEAN, Parc Technologique du Canal, Ramonville St. Agne, France

Key Points:
- Eddy heat fluxes
- Across-stream heat fluxes by the time-mean flow
- Heat flux due to the mean flow in mass-balanced mass balanced regions

Correspondence to:
R. Ferrari,
rflod@locean-ipsl.upmc.fr

Citation:
Ferrari, R., C. Provost, Y.-H. Park, N. Sennéchael, Z. Koenig, H. Sekma, G. Garric, and R. Bourdallé-Badie (2014), Heat fluxes across the Antarctic Circumpolar Current in Drake Passage: Mean flow and eddy contributions, *J. Geophys. Res. Oceans*, *119*, 6381–6402, doi:10.1002/2014JC010201.

Received 3 JUN 2014
Accepted 30 AUG 2014
Accepted article online 5 SEP 2014
Published online 22 SEP 2014

Abstract In contrast to a long-standing belief, observations in the Antarctic Circumpolar Current (ACC) show that mean velocity vectors rotate with depth, thus suggesting a possible importance of the time-mean flow for the local poleward heat transport. The respective contributions of the eddy and mean flows to the heat flux across the ACC in Drake Passage (DP) are investigated using recently acquired and historical time series of velocity and temperature from a total of 24 current meter moorings and outputs of a high-resolution (1/12°) model with realistic topography. Only 11 out of the 24 depth-integrated eddy heat flux estimates are found to be significant, and they are poleward. Model depth-integrated eddy heat fluxes have similar signs and amplitudes as the in situ estimates at the mooring sites. They are mostly poleward or non-significant, with amplitude decreasing to the south. The cross-stream temperature fluxes caused by the mean flow at the moorings have a sign that varies with location and corresponds to the opposite of the vertical velocity estimates. The depth-integrated temperature fluxes due to the mean flow in the model exhibit small spatial scales and are of opposite sign to the bottom vertical velocities. This suggests that the rotation of the mean velocity vectors with depth is mainly due to bottom topography. The rough hilly topography in DP likely promotes the small-scale vertical velocities and temperature fluxes. Eddy heat fluxes and cross-stream temperature fluxes are integrated over mass-balanced regions defined by the model transport streamlines. The contribution of the mean flow to the ocean heat fluxes across the Southern ACC Front in DP (covering about 4% of the circumpolar longitudes) is about four times as large as the eddy heat flux contribution and the sum of the two represent on the order of 10% of the heat loss to the atmosphere south of 60°S.

1. Introduction

In contrast to the Northern Hemisphere where currents transport heat directly to high latitudes, the poleward heat transport in the Southern Ocean is restricted by the near-zonal flow of the Antarctic Circumpolar Current (ACC) which encircles the Antarctic Continent [*Rintoul et al*., 2001] (Figure 1a). However, south of 60°S, the ocean looses between 0.2 and 0.65 PW (1 PW = 10^{15} W) to the atmosphere [e.g., *Large and Yeager*, 2009; *Gordon and Owens*, 1987; *Hastenrath*, 1982] and this heat loss must be balanced by oceanic heat flux across the ACC. Two processes have been put forward for the required oceanic poleward heat flux: a mean meridional flux across the predominantly zonal flow of the ACC and eddy flux resulting from mesoscale eddy activity. The relative importance of each process is still in debate.

High-resolution numerical models have suggested that the poleward heat transport across the ACC south of 45°S is mostly carried by the time-mean horizontal circulation (or standing eddies), with the exception of several regions of energetic mesoscale activity [*Meijers et al*., 2007; *Volkov et al*., 2010]. However, these model results are in contrast with eddy heat flux estimates from in situ observations providing a vertically averaged poleward flux ranging from 10 to 15 kW m^{-2} (kW per unit depth and pathlength of the ACC) [*Bryden*, 1979; *Nowlin et al*., 1985; *Bryden and Heath*, 1985; *Phillips and Rintoul*, 2000; *Walkden et al*., 2008]. The latter local eddy fluxes would be equivalent to 0.8–1.2 PW if extrapolated to the circumpolar belt, thus, in principle, would be more than sufficient to balance the heat loss to the atmosphere south of 60°S. *Sekma et al*. [2013] remarked, however, that most of these eddy heat flux estimates in the order of 10 kW m^{-2} are from the northern flank of the ACC and that the few estimates from the southern flank are much smaller by

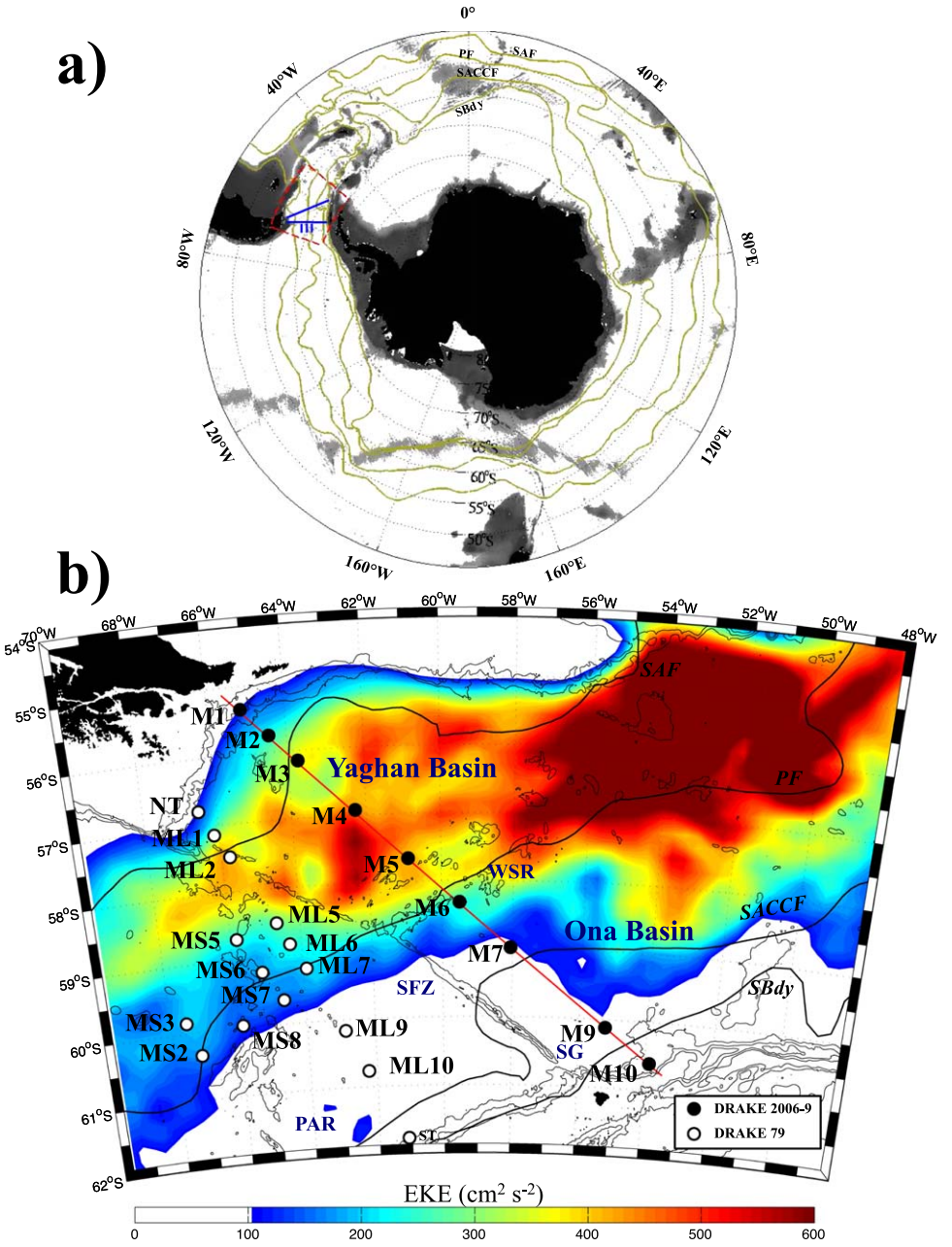

Figure 1. (a) Southern Ocean bathymetry. The solid yellow lines indicate the climatological location of the ACC fonts, according to *Orsi et al.* [1995], form the north to south: SAF, Subantarctic Front; PF, Polar Front; SACCF, Southern ACC Front and SBdy, southern boundary of the ACC. (b) Zoom on the mooring sites. Location of the current meter moorings from DRAKE 2006–2009 (black dots) and DRAKE 1979 (white dots) superimposed on a map of satellite altimetry-derived eddy kinetic energy (EKE) (in $cm^2\ s^{-2}$) from January 2006 to March 2009. The black solid lines indicate the mean location of the major fronts as in Figure 1a. Major ridges or fracture zones are indicated: Shackleton Fracture zone (SFZ); Phoenix Antarctic Ridge (PAR); West Scotia Ridge (WSR) and the Shackleton Gap (SG). Isobaths (1000, 2000, 3000, 4000, and 5000 m) are plotted.

more than one order of magnitude (0.2–0.9 kW m^{-2}). *Sekma et al.* [2013] developed a method based on a shear (thermal wind) reference frame to estimate the across-stream temperature flux due to the time-mean flow. They applied the method to in situ measurements in the Fawn Trough over the Kerguelen Plateau, on the southern flank of the ACC, reporting a large poleward temperature flux caused by the time-mean flow. This poleward temperature flux by the mean flow has been attributed to the anticlockwise turning of the flow direction with decreasing depth, which is associated with significant bottom upwelling generated by strong bottom currents flowing over the sloping topography of the trough. *Sekma et al.* [2013] illustrated

the triple connection between the poleward temperature flux, anticlockwise turning of current with decreasing depth, and bottom upwelling in the Fawn Trough.

The objective of this study is to estimate the eddy and mean flow contributions to the meridional heat flux across the entire ACC breadth in Drake Passage (DP) and examine those contributions in relation to local eddy activity and bottom topography. Indeed, recent 3 year-long in situ time series in DP have shown that the mean flow changes direction with depth [*Ferrari et al*., 2012, 2013] and that the vertical current structure is thus not equivalent barotropic in contrast to early theories [e.g., *Killworth*, 1992; *Killworth and Hughes*, 2002]. The turning of the mean velocity vectors with depth suggests that the mean flow contribution to the meridional heat flux might be significant.

However, point measurements from current meter moorings provide only unit-dependent temperature flux estimates and not meaningful estimates of the heat flux due to the mean flow because the zero on the temperature scale is arbitrary [*Montgomery*, 1974; *Hall and Bryden*, 1982). For a proper estimate of heat flux due to the mean flow, the individual mean temperature fluxes need to be summed over a mass-balanced region. To handle this major constraint of integrating estimates over a mass-balanced region, we use both mooring data and outputs of a high-resolution three-dimensional numerical model of the ocean circulation with realistic topography.

We use in situ temperature and velocity time series from the 2006–2009 DRAKE experiment (DRAKE 2006–2009) and from the year-long historical DRAKE 1979 experiment [*Ferrari et al*., 2012, 2013; *Whitworth et al*., 1982]. The DRAKE 2006–2009 mooring line was located downstream of the Shackleton Fracture Zone (SFZ), a major ridge across DP reaching up to 1500 m from the surface in the south, whereas the data from the DRAKE 1979 came from upstream of the SFZ (Figure 1b). The combined data sets enable documenting heat fluxes in contrasted topographic and eddy activity situations, the mesoscale eddy activity being much larger in the north of the Passage than in the south (Figure 1b). The DRAKE 1979 mooring data had already been used to estimate eddy heat fluxes by *Nowlin et al*. [1985] and are used here to estimate the cross-stream temperature flux due to the mean flow. Mooring data are used to assess the validity and limitations of the outputs from the high-resolution numerical model. The model outputs are used to help interpreting the spatial structures in which the point measurement estimates are embedded and to compute heat fluxes over mass-balanced regions.

In situ data sets and model outputs are presented and compared in section 2. Section 3 is devoted to eddy heat fluxes: eddy heat fluxes from the recent DRAKE 2006–2009 data set are estimated and compared to those from the Drake 1979 experiment [*Nowlin et al*., 1985]; model eddy heat fluxes are compared to in situ estimates and discussed. Section 4 deals with heat fluxes due to the mean flow. It first recalls the necessity of integrating over mass-balanced regions to obtain meaningful estimates of heat fluxes due to the mean flow and the method used to produce estimates of vertical velocities and of cross-stream heat fluxes caused by the mean flow. Results for the two data sets and model outputs are shown and the validity of the upper-mentioned triple connection described in *Sekma et al*. [2013] is verified both with the in situ data and model outputs. Section 5 discusses the results, compares eddy heat fluxes and heat fluxes due to the mean flow over mass-balanced regions and draws perspectives.

2. Data Sets and Model Outputs

2.1. Three Year-Long (2006–2009) Recent Mooring Data in Drake Passage

The current meter array made up of nine moorings (DRAKE 2006–2009; M1 through M10, M8 being lost) was located under the Jason altimeter satellite track #104, parallel to the DRAKE 1979 main line moored array [*Hofmann and Whitworth*, 1985] but on the eastern side of the SFZ (Figure 1). These moorings gathered 3 years (2006–2009) of current and temperature measurements in the Yaghan Basin [*Ferrari et al., 2*012] and 2 years (2006–2008) in the Ona Basin [*Ferrari et al*., 2013]. All the moorings (except the northern one) carried three current meters at approximately 500, 1000, and 2500 m depths. Hydrographic data were gathered along the section during the deployment and recovery cruises [*Provost et al*., 2011].

The records of raw velocity and temperature data were low-pass filtered with a cutoff period of 25 h to remove inertial and tidal variations and then resampled at a daily rate. A mooring motion-correction

Table 1. Statistics of the DRAKE 2006–2009 Current Meter Moorings (From January 2006 to March 2009)[a]

N°	Observations	$\overline{P}$ (dbar)	$\|\overline{V}\|$ (cm s^1)	$\varphi(\|\overline{V}\|)$ (°)	Major Axis (cm s^{-1})	Minor Axis (cm s^{-1})	$\overline{T}$ (°C)	$\sigma(T)$ (°C)
M1-1	1134	60	20.5	51.2	22.5	12.3	5.36	0.80
M1–2	1134	430	16.4	50.9	17.7	8.8	4.76	0.21
M1–3	869	935	12.0	47.3	12.8	5.1	3.36	0.22
M2-1	343	415	37.7	45.8	23.5	15.9	4.03	0.72
M2-2	343	920	23.6	48.0	13.6	10.2	2.99	0.35
M2–3	343	1970	11.8	46.2	8.4	8.2	2.03	0.12
M3-1	1156	335	20.85	25.3	20.7	18.0	3.20	0.69
M3-2	344	425	20.2	22.3	18.7	17.9	3.14	0.58
M3-3	1156	910	14.7	14.9	12.7	11.6	2.72	0.24
M3–4	1156	1900	10.7	13.0	9.8	8.0	1.94	0.12
M3–5	344	2890	12.7	12.7	10.9	6.3	1.32	0.15
M4-1	1143	470	7.5	−41.3	21.3	18.1	3.06	0.53
M4-2	1143	980	10.6	−55.4	15.9	14.1	2.58	0.23
M4-3	1143	2475	13.5	−80.5	10.9	10.3	1.51	0.14
M5-1	1123	540	17.1	68.9	18.1	14.5	2.79	0.34
M5-2	1123	1040	11.0	64.7	10.7	8.1	2.23	0.21
M5-3	1123	2555	3.7	95.7	7.2	3.6	1.22	0.19
M6-1	805	235	21.5	43	14.4	11.9	1.94	0.29
M6-2	805	820	13.5	38	8.3	6.3	1.92	0.19
M6-3	805	2410	5.7	18	5.3	3.7	0.81	0.17
M7-1	690	460	0.7	105	7.2	6.2	1.82	0.19
M7-2	690	980	2.2	187	6.2	5.6	1.45	0.15
M7-3	803	2515	3.9	202	6.4	5.8	–	–
M9-2	800	1040	10.2	325	10.6	8.6	1.24	0.23
M9-3	800	2520	8.7	312	9.0	8.2	0.27	0.09
M10-1	438	460	2.4	55.4	8.6	4.0	0.41	0.56
M10-2	774	990	1.5	85.5	7.4	4.2	–	–
M10-3	324	2560	3.8	166.4	5.8	3.5	−0.03	0.04

[a] $\overline{P}$ is the mean pressure averaged over the record length. $\|\overline{V}\|$ is the modulus of the time average of the velocity, and $\varphi(\|\overline{V}\|)$ is the mean velocity direction. Major and minor axes are those of the velocity standard deviation ellipses. The mean velocity direction is relative to the geographical north (positive values are clockwise). $\overline{T}$ and $\sigma(T)$ represent the mean and standard deviation temperature, respectively.

scheme adapted from *Cronin and Watts* [1996] was applied allowing an interpolation (and extrapolation) of the velocity and temperature measurements at fixed depths. Details of this correction method can be found in *Ferrari et al.* [2012]. The velocity and temperature time series from January 2006 to April 2009 are shown in Figure 2. Basic statistics are summarized in Table 1. Measurements reveal a vertical consistency of the velocity and temperature variations with a significant correlation on the vertical ($r > 0.6$ for velocity variations and $r > 0.45$ for temperature variations). The standard deviation ellipse axes are roughly parallel in the vertical for all moorings (Figure 3 and Table 1). However, a clockwise rotation of the mean velocity vector with decreasing depth suggests downwelling through the entire water column at M3, M4, M6, and M9, while the anticlockwise rotation at M5 and M10 indicate upwelling [*Ferrari et al.*, 2012, 2013]. Mean velocities are larger than their standard deviation at four mooring sites: at M2, which evidenced the strong eastward flow associated with the Subantarctic Front (SAF), at M5 and M6, which recorded the eastward flow associated with the Polar Front (PF) and the northern branch of the Southern Antarctic Circumpolar Current Front (SACCF) over the West Scotia Ridge (WSR), and at M9, which sampled a northwestward flow associated with the southern branch of the SACCF. The velocity variance ellipses are close to circular except over the continental slope where they are stretched in the direction of isobaths (M1 and M10) (see Figure 3 and Table 1).

A principal component analysis has provided a quantitative overview of the vertical structure of the velocity variations [see *Ferrari et al.*, 2012, 2013]. Recall that the three leading empirical orthogonal functions (EOF) explain between 93% and 99% of the in situ velocity variance. The first EOF explains between 50% and 74% of the variance and shows a consistent orientation and a slight decrease in amplitude with depth for each mooring. At M6, we note a slight counterclockwise veering below 1000 m. The second mode accounts for a smaller fraction of the variance (between 21% and 41%) and shows parallel vectors at all depths and a surface intensification. The third EOF explains between 3% and 9% and corresponds to a baroclinic component. An analysis of the spectral content of the time series has shown [see also *Ferrari et al.*, 2012, 2013] that most of the energy was found at periods between 5 and 80 days, the smallest periods being observed at

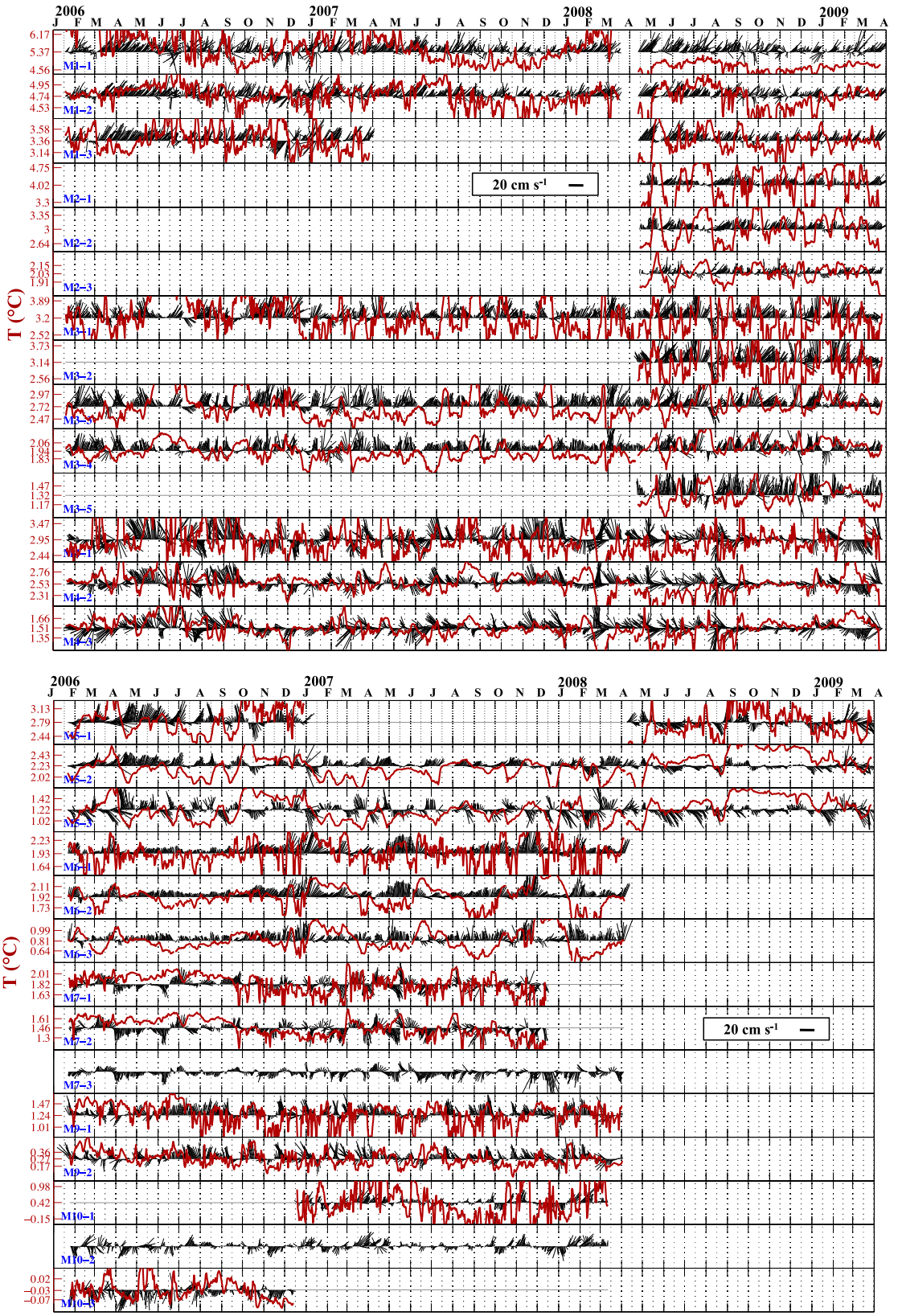

Figure 2. Stick plots of velocity (cm s^{-1}) and temperature (in red) time series from DRAKE 2006–2009 current meter moorings. Velocity and temperature current meters data were corrected applying a mooring motion-correction scheme adapted from *Cronin and Watts* [1996].

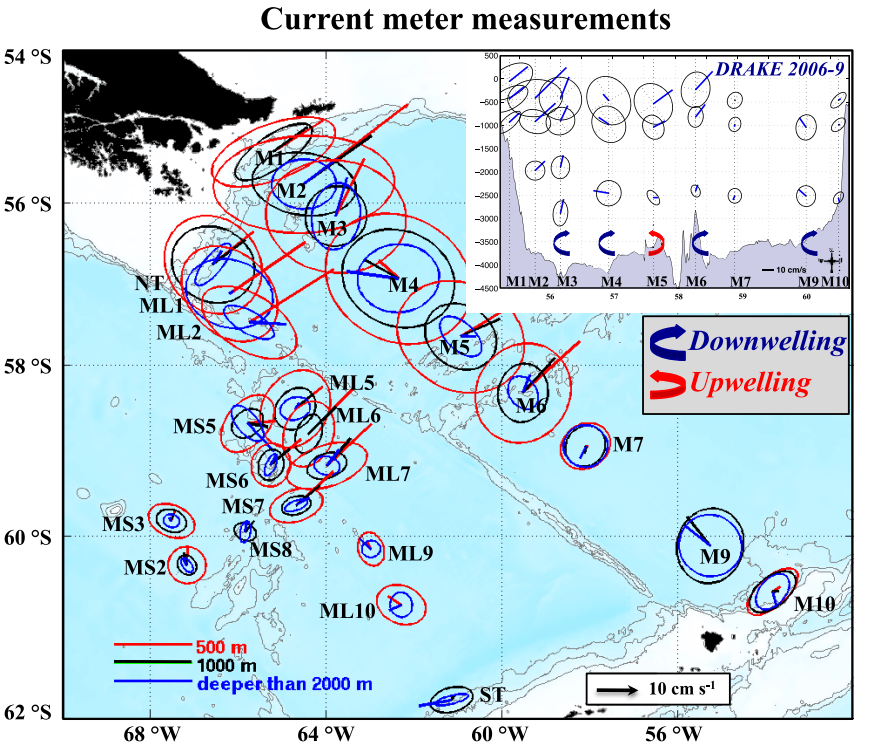

Figure 3. Time-mean velocity vectors and velocity standard deviation ellipses are calculated from current meter measurements at 500 m in red, at 1000 m in black, and deeper than 2500 m in blue. In the top corner: vertical section of time-mean velocity vectors and standard deviation ellipses from the DRAKE 2006–2009 current meter array over the 3 year period: from January 2006 to March 2009. The bottom topography is indicated in solid gray. Velocity scale and compass directions are indicated in the bottom right corner. The clockwise rotation of the mean velocity vector with decreasing depth is indicative of downwelling while the anticlockwise rotation indicates upwelling.

M1 and associated with intermittent continental trapped waves, and the largest periods being associated with meanders of the PF at M6.

2.2. Times Series of Velocity and Temperature From DRAKE 1979 Experiment

Velocity and temperature measurements from the DRAKE 1979 moorings are available at the Oregon State University buoy group database (http://cmdac.oce.orst.edu/). The CTD data from DRAKE 1979 were obtained from the National Oceanographic Data Center (NODC http://www.nodc.noaa.gov/). These moorings were part of the International Southern Ocean Studies (ISOS). ISOS was a landmark experiment that laid much of the foundations of our current understanding of the ACC in DP. The DRAKE 1979 current observations have indicated that bottom topography plays an important role in the flow variability [*Hofmann and Whitworth*, 1985; *Klinck*, 1985]. These have led to estimates of the ACC transport [e.g., *Whitworth*, 1983] and a characterization of eddy heat fluxes across DP [*Nowlin et al*., 1985].

The DRAKE 1979 mooring array in place on the western side of the SFZ consisted of two major parts: a main line array (ML) and a cluster of moorings in the central passage (MS) (see Figure 1b). The MS moorings were located in the central passage where the bottom bathymetry is quite rugged, with a line of seamounts of the Phoenix Antarctic Ridge, stretching roughly in the north-south direction between longitudes 65° W and 66° W.

We used the year-long velocity and temperature records from 40 Aanderaa current meters; 17 instruments from the MS, 16 from ML, 5 from NT (northern continental slope), and 2 from ST (southern continental slope) to compute cross-stream heat fluxes caused by the mean flow. Current meters were positioned at nominal depths of 500 m and 2500 m on all moorings and at 1400 m on the MS moorings. Mean velocities do slightly rotate with depth as noted by *Bryden* [1979] and *Nowlin et al*. [1985] and the sense of rotation varies with location (Figure 3). The anticlockwise rotation of the mean velocity vector with decreasing depth at ML2 is indicative of upwelling, while the clockwise rotation at ML7 indicates downwelling. The axes of the velocity standard deviation ellipses are smaller in the south than in the north and are in general smaller than those observed downstream of the SFZ in 2006–2009 at the same latitude (see Figure 3).

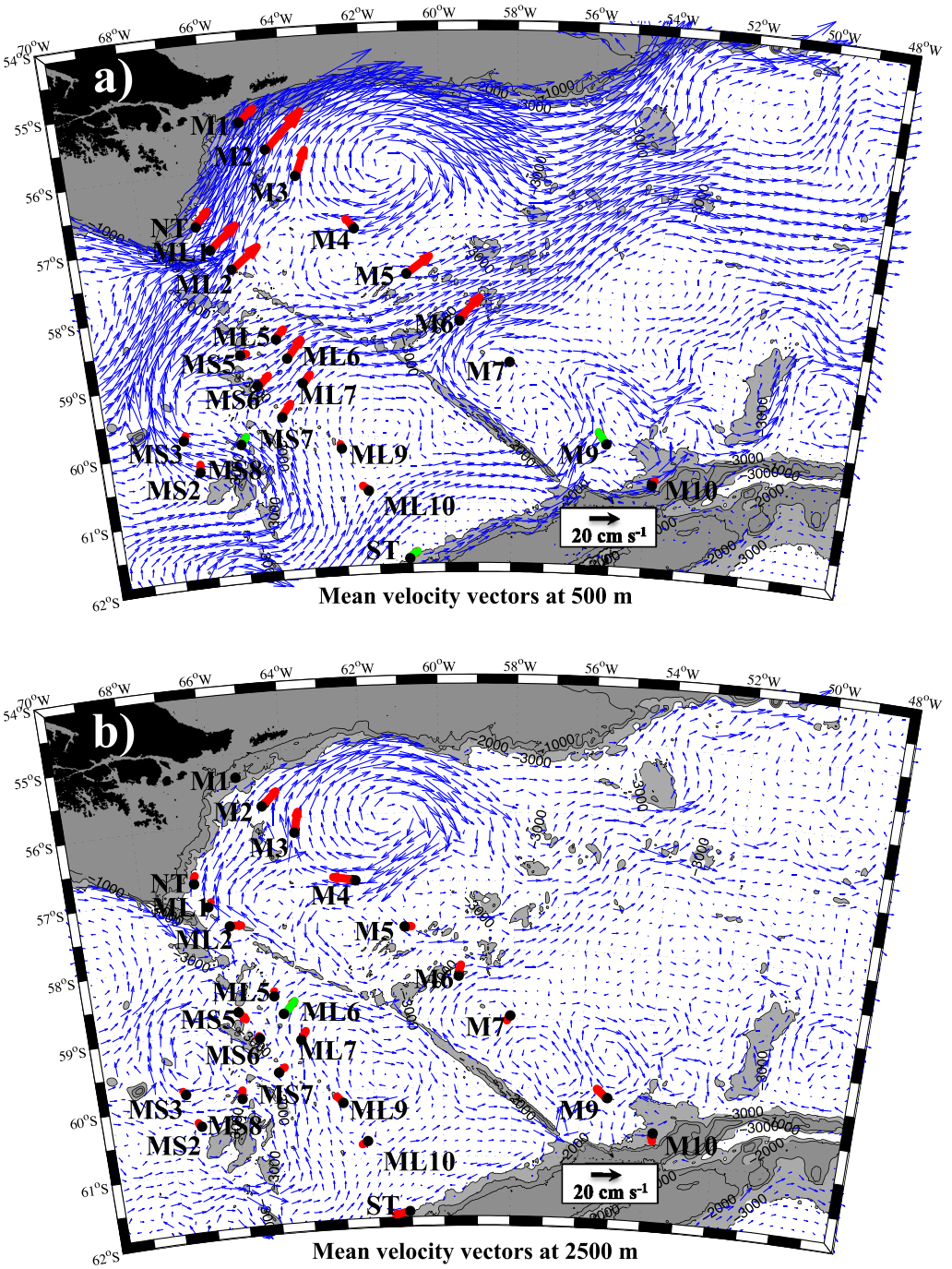

Figure 4. (a) Mean velocity vectors at 500 m from Orca 12 model outputs (blue arrows) and from current meter moorings (~500 m, red arrows). (b) Mean velocity vectors at 2500 m from Orca 12 model outputs (blue arrows) and from current meter moorings (~2500 m, red arrows). Mean flow from Orca 12 model outputs were estimated during DRAKE measurements period (2006–2009). The three green arrows at MS4, ST, and M9 in Figure 4a correspond to the upper level at those moorings which is about 1000 m (not 500 m). The green arrow at ML6 in b corresponds to that mooring lower level that is 1300 m. Bottom topography shallower than 3000 m is shaded in gray.

2.3. Three-Years (2006–2009) of High-Resolution Ocean Circulation Model Outputs

The model outputs used were created from the ORCA 12 ocean model with a 1/12° horizontal and a 3 day temporal resolution (Mercator Océan, Toulouse, France). This model is based on the NEMO code [*Madec*, 2008], which resolves the primitive equations. The ORCA 12 ocean model is coupled to the LIM (Louvain Ice Model) sea ice model [*Fichefet and Maqueda*, 1997]. The 50 level vertical discretization retained for

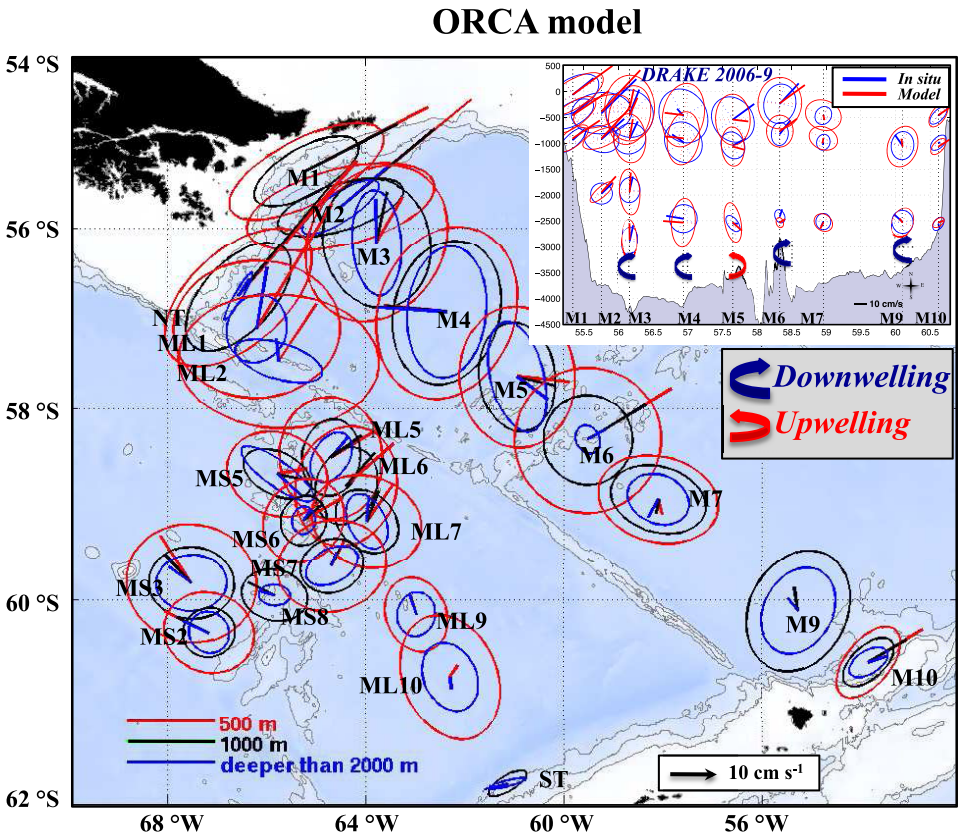

Figure 5. Time-mean velocity vectors and velocity standard deviation ellipses obtained from Orca 12 model outputs at 500 m in red, 1000 m in black, and 2500 m in blue. In the top corner: along the DRAKE 2006–2009 section: time-mean velocity vectors and standard ellipses from Orca 12 model outputs (in red) and from DRAKE current meter array (in blue) from January 2006 to March 2009. The bottom topography is indicated in solid gray. Velocity scale and compass directions are indicated in the bottom right corner. The clockwise rotation of the mean velocity vector with decreasing is indicative of downwelling while the anticlockwise rotation indicates upwelling.

operational applications by Mercator Océan has a 1 m resolution near the surface decreasing down to 450 m at the bottom, and 22 levels stacked in the upper 100 m.

For this simulation, ORCA12 was forced by the bulk CORE formulation [*Large and Yeager*, 2009] using the forcing files from the ERA-interim reanalysis [*Dee et al.*, 2011]. The frequency of the forcing is 3 h for the 10 m wind, the 2 m air temperature, and the 2 m-specific humidity. Long-wave and shortwave radiative fluxes and precipitations (solid and liquid) have a daily frequency. An analytical diurnal cycle [*Bernie et al.*, 2005] is applied to the shortwave flux, whose large-scale bias was removed considering GEWEX observations. There is no sea surface salinity restoring on top of the freshwater fluxes.

2.4. Comparison of the Model Outputs With In Situ Data

The model outputs were carefully compared to the concomitant DRAKE 2006–2009 data and to a lesser degree with the nonconcomitant DRAKE 1979 data. Some model features are remarkably in agreement with in situ observations while others do differ significantly. Differences are pointed out as they may explain discrepancies between heat flux estimates.

The major differences between the model mean flow and the DRAKE 2006–2009 data are found at the two steep continental slopes showing too large mean velocities (M1 and M10). Maps of the mean flow at 500 m and at 2500 m (Figure 4) show a general agreement with the concomitant DRAKE 2006–2009 mean velocities, particularly with the spectacular cyclonic recirculation in the Yaghan Basin described in *Ferrari et al.* [2012]. Differences with the nonconcomitant DRAKE 1979 data are important on the slope (ML1 and ML2) where model velocities are larger with a direction off by 50° at 500 m and even opposite at 2500 m at ML2, as well as in the west at MS2, MS3, MS8, and ML10 (Figure 4). Model mean velocity vectors do rotate slightly with depth (Figure 5) and the sense of rotation is similar to that found in the DRAKE 2006–2009 observations

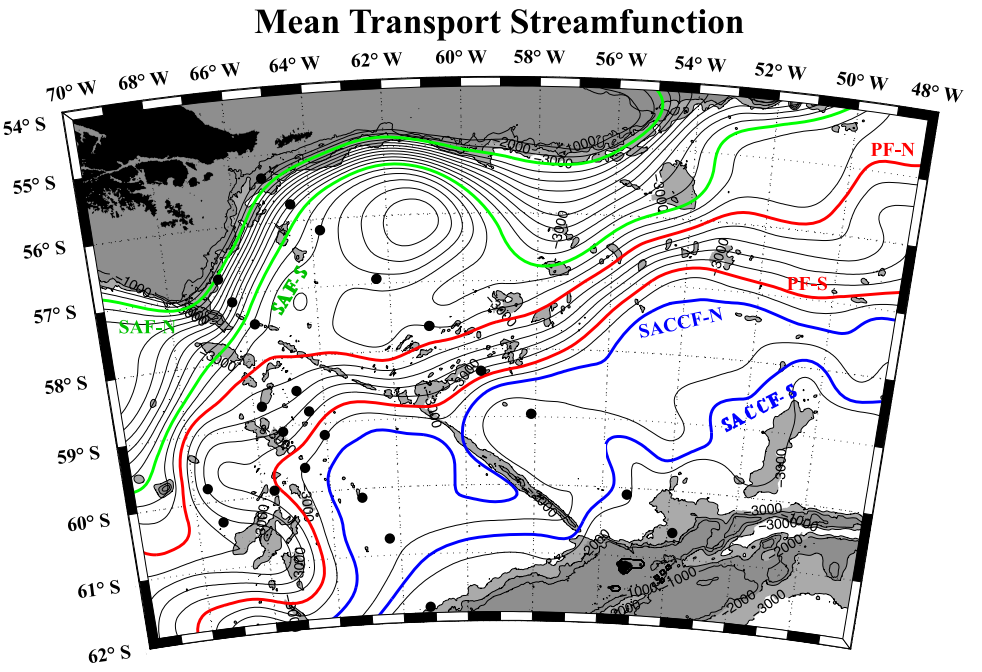

Figure 6. 3 year (2006–2009) mean transport stream function from model outputs. Streamlines between −85 and 40 $m^4 s^{-1}$ are plotted in black solid lines with a 5 $m^4 s^{-1}$ step. Major branches of the SAF, PF, and SACCF are identified with a green, red, and blue solid lines, respectively.

(e.g., M3, M4, M6, M9) (Figure 5). Model derived velocity standard deviation ellipses are generally larger than those from the two in situ data sets (Figure 5 compared with Figure 3).

Mean model temperatures (not shown) tend to be smaller than mean in situ temperatures in the Yaghan Basin and larger in the Ona Basin. The mean of the absolute differences is 0.25°C. Temperature standard deviations tend to be larger in the model than in the observations at the four northern mooring sites (M1 through M4) and smaller at the southern sites (M5 to M10). The mean difference in temperature standard deviation between model and observations is 0.07°C.

Model transport streamlines, lines that are tangential to the vertically integrated mean velocity vector at each point, are plotted in Figure 6. They correspond to isolines across which the volume flux is zero, by definition, much the same as the transport across the southernmost streamline, the Antarctic coast, is zero. The model transport streamlines corresponding to the classical hydrographic fronts, the SAF-N, SAF-S, PF-N, PF-S, SACCF-N, and SACCF-S as described in *Provost et al*. [2011], are used as boundaries to define the mass-balanced regions: a "SAF mass-balanced region" between the two SAF fronts, a "PF mass-balanced region" between the two PF fronts, and a "SACCF mass-balanced region" between the two SACCF fronts (Figure 6). Heat fluxes due to the mean flow will be computed over these mass-balanced regions and compared to eddy heat fluxes averaged over the same regions.

3. Eddy Heat Fluxes

3.1. Method

To estimate the across-stream eddy heat flux, it is necessary to determine the most adequate coordinate system and time scales to isolate the mesoscale variability. *Nowlin et al*. [1985] proposed a band-pass width of 40 h to 90 days. The latter has been commonly accepted [e.g., *Phillips and Rintoul*, 2000; *Walkden et al*., 2008; *Sekma et al*., 2013] and it was adopted here after a careful examination of temperature and velocity cross spectra.

The directions of along-stream or cross-stream can be determined using two kinds of coordinate systems: time-invariant and time-varying systems. The time-invariant coordinate system called "geographic coordinate system" [*Bryden*, 1979] defines along-stream as being directed along the time-mean flow and cross-

stream is 90° to the left of along-stream. For the time-varying coordinate systems, we used the "90d-LP coordinate system" based on a mean flow with slowly varying direction, derived from the 90 day low-passed velocity [*Nowlin et al*., 1985]. The cross-stream velocity is defined to be positive to the left of the 90 day low-passed direction. We use here the same methodology as described in *Sekma et al*. [2013], which is briefly summarized below.

For the geographical coordinate system, the cross-stream velocity time series $V(t)$ is obtained as:

$$V(t)=v(t)\cos(\varphi)-u(t)\sin(\varphi) \tag{1}$$

where $\varphi=\tan^{-1}(\overline{u}/\overline{v})$ is the angle of the time-mean current direction relative to the positive x coordinate (east). Low-frequency variations of periods greater than 90 days (green lines in Figure 7) are filtered out from the daily time series using a Gaussian filter [*Park and Gambéroni*, 1995] to retain mesoscale temperature and velocity anomaly time series, $T'(t)$ and $V'(t)$, having periods between 40 h and 90 days. This yields the correlation time series of the two parameters $T'V'$. The mean eddy heat flux $\overline{Q}'$ is then obtained by using $\overline{Q}'=\rho_0 C_p\overline{V'T'}=41.4\overline{V'T'}$ [kW m^{-2}]. (Note that the units used in this formula are cm s^{-1} for velocity and °C for temperature.)

Similar procedures are applied to the 90d-LP coordinate system (Figure 7), except for φ which is instead defined as the time-varying daily angles of the 90d-LP velocity vectors relative to the positive x coordinate.

The statistical significance of time-mean eddy heat fluxes is tested following the method employed by *Nowlin et al*. [1985]. For testing zero correlation at a 95% confidence level, the method compares the zero-lag cross-correlation between $V'(t)$ and $T'(t)$ with its standard error (*SE*) multiplied by 2. The *SE* is estimated from the number of degree freedom N^*, with $SE=1/\sqrt{N^*}$, where N^* is equal to the length of the time series divided by the integral timescale τ which is defined by:

$$\tau=\sum_{j=-M}^{M} C_{vv}(j\Delta t)C_{TT}(j\Delta t)\Delta t \tag{2}$$

where C_{vv} and C_{TT} are the autocorrelation functions of $V'(t)$ and $T'(t)$, respectively and M equal to 20% as in *Nowlin et al*. [1985].

3.2. Eddy Heat Fluxes From DRAKE 2006–2009

Record-length mean values of eddy heat flux are presented in Tables 2, with eddy heat flux calculated in geographic coordinates in the fourth column and that from the 90d-LP method in the fifth column. Both methods provide similar and consistent results. Only a few eddy heat fluxes are significantly different from zero at a 95% confidence level (6 out of 21 estimates for the 2006–2008 period and 1 out of 17 estimates in the 2008–2009 period). The eddy heat fluxes are generally poleward, although we note several statistically nonsignificant equatorward fluxes. Eddy heat fluxes range from +21.2 to −92.1 kW m^{-2}. Large significant poleward eddy heat fluxes occur at the near-surface current meter level in the northern passage at M1 (at 60 db), at depth in the Polar Frontal Zone (below 2500 db at M5 and 800 db at M6), and through the entire water column at M9 corresponding to the SACCF. We observe considerable differences in eddy heat flux estimates between the 2006–2008 and 2008–2009 periods, indicating a significant year-to-year variability in local eddy heat flux.

3.3. Comparison With DRAKE 1979 Eddy Heat Fluxes

The estimates from the DRAKE 2006–2009 experiment are of the same order of magnitude as those from the DRAKE 1979 experiment as calculated by *Nowlin et al*. [1985] and reported in Table 3 (column 4). The DRAKE 1979 eddy heat flux estimates have a large range of values (+5.5 to −64.3 kW m^{-2}) are generally poleward and a few nonsignificant flux values are equatorward. Only 15 out of a total of 50 estimates from the DRAKE 1979 are statistically significant. Large significant poleward fluxes occur in the northern passage. Eddy heat fluxes are intensified in the upper layer and show a considerable year-to-year variability. Our estimates from the DRAKE 2006–2009 are qualitatively consistent with those from the DRAKE 1979, confirming most of the statements given in *Nowlin et al*. [1985].

The only notable difference between the DRAKE 1979 eddy heat flux estimates upstream of the SFZ and the ones presented here downstream of the SFZ is the presence of significant and relatively large eddy

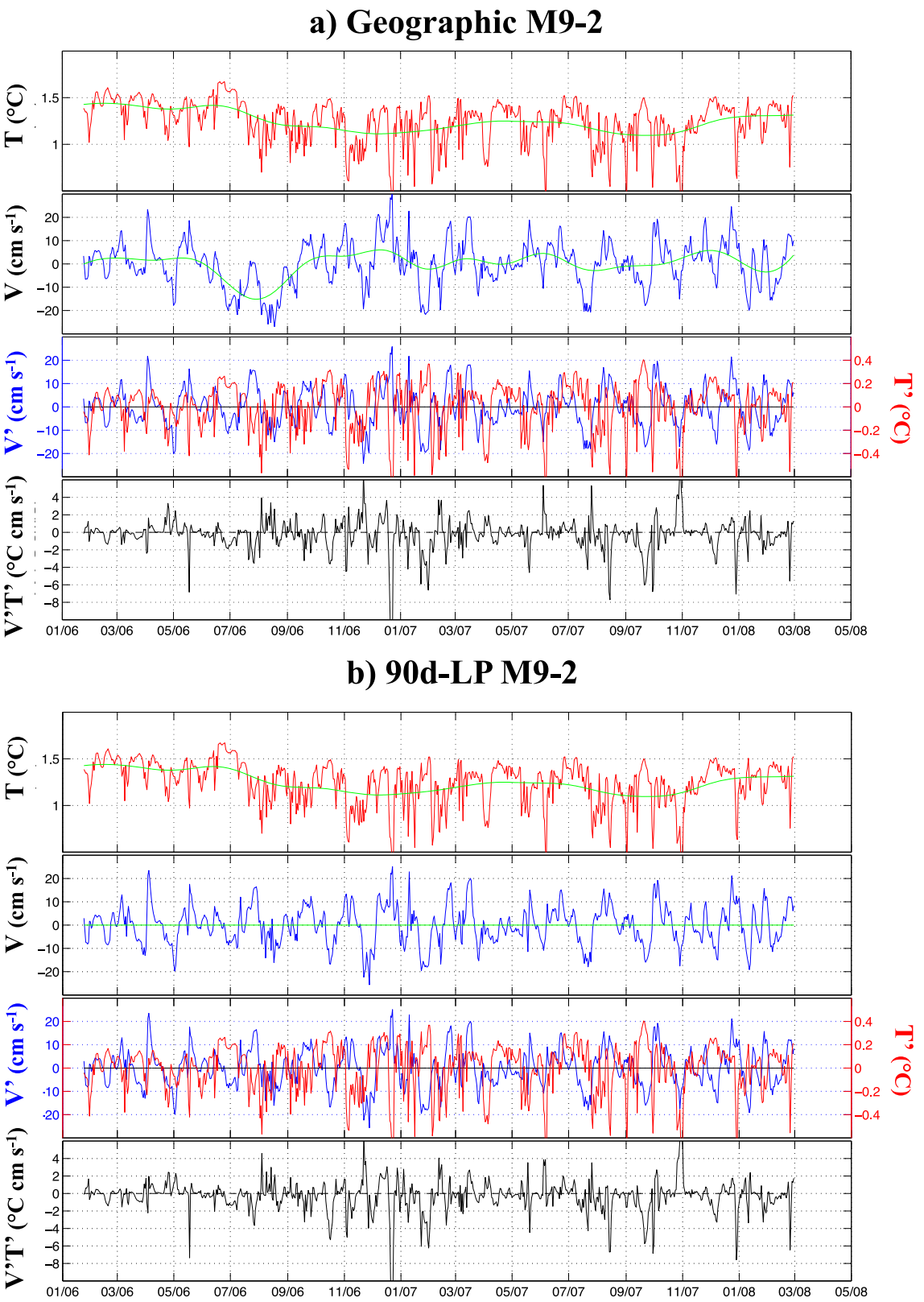

Figure 7. A typical example at M9, illustrating (top to bottom in each series) how time series of "eddy" temperature *T′* and "eddy" cross-stream velocity *V′* are obtained to compute their product *T′V′* in two different coordinates: (a) geographic coordinates and (b) 90d-LP systems. Temperature (*T*) and velocity (*V*) time series have been filtered at 40 h, from which the 90-day low-pass filtered series (green lines superimposed on the *T* and *V* curves) are subtracted to get the band-pass (40 h–90 days) filtered *T′* and *V′*.

Table 2. Estimates of Heat Flux for All Moorings of DRAKE 2006–2009 (in kW m^{-2}) and Vertical Velocity (in m day^{-1}) During 2006–2008 (a) and 2008–2009 (b) Periods[a]

Mooring	Pressure (dbar)	Record Length (days)	Eddy Heat Flux (Geographic 90d_LP)	Eddy Heat Flux (90d-LP)	Mean Vertical Velocity (m day^{-1})	Mean Temperature Flux (Shear)
During 2006–2008						
M1-1	60	433	*−92.11*	*−71.49*	*50.9 ± 17.7*	*−1999.0 ± 386.6*
M1–2	380		−1.78	2.48	*−32.3 ± 9.5*	*989.7 ± 141.9*
M1–3	860		−4.88	−2.20		
Mean M1			**−6.4**	**−4.9**	**0.9**	**−70.8**
M3-1	380	318	−4.79	−0.14	*−17.7 ± 5.2*	*400.5 ± 142.1*
M3-3	910		0.49	3.78	*−6.9 ± 1.7*	*236.1 ± 53.7*
M3–4	1920		2.36	3.03		
Mean M3			NS	NS	**−8.5**	**311.04**
M4-1	430	772	−31.30	−35.00	−8.6 ± 7.8	210.7 ± 193.6
M4-2	960		4.71	−8.19	−51.8 ± 15.6	569.8 ± 152.3
M4-3	2450		4.63	0.28		
Mean M4			NS	NS	**−31.5**	**337.5**
M5-1	570	771	−25.49	−32.35	−40.6 ± 29.4	391.5 ± 306.9
M5-2	1085		−13.20	−14.56	24.2 ± 16.4	−141.1 ± 77.9
M5-3	2645		*−21.35*	*−18.71*		
Mean M5			**−14.7**	**−12.8**	NS	NS
M6-1	237	341	3.82	−0.46	*−29.1 ± 6.0*	*244.2 ± 41.8*
M6-2	828		*−11.19*	*−11.84*	*−27.7 ± 6.0*	*165.1 ± 12.7*
M6-3	2449		*−10.82*	*−11.51*		
Mean M6			**−9.9**	**−10.5**	**−25.4**	**190.8**
M7-1	467	677	1.45	−1.73	−0.9 ± 8.7	47.3 ± 29.2
M7-2	991		0.11	−0.84	–	–
M7-3	2553		–	–		
Mean M7			NS	NS	NS	NS
M9-2	1057	767	*−11.38*	*−13.27*	*−33.7 ± 7.8*	*101.4 ± 12.0*
M9-3	2560		*−4.95*	*−5.10*		
Mean M9			**−7.6**	**−8.5**	**−33.7**	**101.4**
M10II-1	–	280	–	–	–	–
M10II-2	1068		–	–		
M10II-3	2598		1.26	1.28		
M10III-1	466	424	6.23	10.18	–	–
M10III-2	979		–	–		
M10III-3	–		–	–		
During 2008–2009						
M1-1	60	319	1.41	2.89	*23.3 ± 9.5*	*−672.1 ± 271.3*
M1–2	490		2.05	2.16	*−14.7 ± 7.8*	*497.5 ± 185.8*
M1–3	1030		−0.08	0.90		
Mean M1			NS	NS	**2.0**	**74.3**
M2-1	300	318	10.20	−7.84	*27.7 ± 16.4*	*−363.5 ± 70.9*
M2-2	430		−12.05	−19.78	*−15.6 ± 6.1*	*322.9 ± 30.9*
M2–3	2000		−5.77	−6.96		
Mean M2			NS	NS	**−10.4**	**116.7**
M3-1	300	318	−48.91	−48.62	*−13.0 ± 4.3*	*1119.7 ± 64.7*
M3-2	430		−40.25	−35.93	*15.6 ± 3.5*	*−1592.5 ± 38.4*
M3-3	930		−6.57	−7.30	*−8.6 ± 2.6*	*698.1 ± 59.9*
M3–4	1940		−1.23	−0.36	*−19.0 ± 4.3*	*236.0 ± 36.6*
M3–5	2940		−6.32	−5.41		
Mean M3			NS	NS	**−7.3**	**275.1**
M4-1	520	319	1.00	−27.53	−0.9 ± 8.65	−2.3 ± 100.8
M4-2	1020		−11.56	−17.91	*−22.5 ± 9.5*	*366.4 ± 134.8*
M4-3	2540		*−13.00*	*−14.14*		
Mean M4			**−7.8**	**−8.5**	**−13.5**	**207.1**
M5-1	520	319	21.20	8.79	4.3 ± 7.8	−116.8 ± 96.7
M5-2	1020		6.51	3.17	6.9 ± 3.5	−149.3 ± 76.4
M5-3	2540		1.47	0.89		
Mean M5			NS	NS	NS	NS

[a]Heat fluxes due to the mean flow are estimated in shear coordinate system, while eddy heat fluxes are in Geographic and 90d-LP coordinate system. Significant flux at a 95% confidence levels are shown in italic. Depth-averaged heat fluxes for each mooring are in bold.

fluxes (−13.3 and −5 kW m^{-2}) in the southern DP at M9 at two levels (1057 and 2560 dbar) from the DRAKE 2006–2009. Indeed, our M9 reveals an elevated eddy activity with large velocity standard deviation ellipses, significantly larger than those from DRAKE 1979 on the other side of the SFZ (see Figure 3).

Table 3. Estimates of Heat and Temperature Flux (in kW m^{-2}) and Vertical Velocity (in m day^{-1}) From DRAKE 1979 Data[a]

Mooring	Depth [*Nowlin et al.* 1985] (m)	Record length [*Nowlin et al.* 1985] (days)		Eddy Heat Flux [*Nowlin et al.* 1985] (90d-LP)	Mean Vertical Velocity (m day^{-1})	Mean Temperature Flux (Shear)
NT-1	590 [645]	176	[174]	*−44.4 [−49.0]*	3.4 ± 3.1	−146.8 ± 174.5
NT-2	900 [944]		[403]	*−18.9 [−20.8]*	*−7.1 ± 3.3*	*214.9 ± 72.9*
NT-3	1315 [1349]		[187]	−0.7 [−2.0]	0.4 ± 2.2	−47.1 ± 67.9
NT-4	1651 [1651]		[403]	2.3 [0.3]	*−4.4 ± 1.9*	*84.4 ± 34.4*
NT-5	2605 [2637]		[403]	2.3 [0.6]		
Mean NT				**−12.3 [−13.6]**	**−2.5**	**85.7**
ML1-1	525 [802]	405	[398]	*−78.3 [−64.3]*	*2.3 ± 0.9*	*−225.2 ± 90.5*
ML1–2	2525 [2800]		[400]	−1.65 [−0.5]		
Mean ML1				**−16.3 [−13.4]**	**2.3**	**−225.2**
ML2-1	565 [900]	388	[383]	13.0 [8.0]	28.8 ± 5.6	−711.1 ± 85.3
ML2-2	2535 [2711]		[399]	*−9.8 [−8.8]*		
Mean ML2				**−7.6 [−6.8]**	**28.8**	**−711.1**
ML5-1	605 [644]	342	[397]	3.0 [2.4]	−0.1 ± 0.7	26.8 ± 33.3
ML5-2	1310 [1344]		[397]	−1.2 [−0.3]	−0.7 ± 1.9	34.6 ± 29.1
ML5-3	2610 [2644]		[340]	−0.5 [−1.3]		
Mean ML5				NS [NS]	NS	NS
ML6-1	620 [685]	398	[395]	−0.5 [−0.3]	*1.1 ± 0.4*	*−91.1 ± 36.9*
ML6-2	1320 [1384]		[395]	−1.4 [−1.2]		
Mean ML6				NS [NS]	**1.1**	**−91.1**
ML7-1	500 [575]	346	[342]	*−1.9 [−1.7]*	*−1.7 ± 0.6*	*89.0 ± 27.4*
ML7-2	1220 [1290]		[395]	*−3.3 [−2.9]*	1.1 ± 1.8	−11.8 ± 29.4
ML7-3	2540 [2593]		[395]	*−3.2 [−3.2]*		
Mean ML7				**−2.6 [−2.5]**	**−9.7**	**31.4**
ML9-1	590 [608]	382	[319]	0.12 [0.2]	*−0.3 ± 0.1*	*44.9 ± 14.3*
ML9-2	2640 [2665]		[384]	*−0.8 [−1.0]*		
Mean ML9				**−0.6 [−0.8]**	**−0.3**	**44.9**
ML10-1	475 [498]	393	[391]	−0.8 [−1.1]	−0.4 ± 0.3	87.1 ± 59.1
ML10-2	2530 [2575]		[391]	−0.4 [−0.3]		
Mean ML10				[NS]	NS	NS
ST-2	1390 [1401]	392	[389]	*−3.1 [−3.5]*	−0.1 ± 0.4	13.8 ± 18.7
ST-3	2670 [2701]		[389]	0.3 [0.1]		
Mean ST				**−1.6 [−1.8]**	NS	NS
MS1-1	675 [685]	358	[236]	0.1 [−]	−0.2 ± 0.3	37.3 ± 18.8
MS1–2	1370 [1383]		[355]	−0.2 [−0.7]	0.4 ± 0.9	−16.7 ± 21.3
MS1–3	2660 [2685]		[355]	−0.3 [−0.4]		
Mean MS1				NS [NS]	NS	NS
MS2-1	790 [800]	358	[355]	−1.1 [0.0]	*−1.1 ± 0.3*	*127.9 ± 30.2*
MS2-2	1470 [1485]		[355]	−0.4 [0.1]	*−1.3 ± 0.4*	*60.6 ± 20.9*
MS2–3	2760 [2785]		[355]	−0.2 [0.0]		
Mean MS2				NS [NS]	**−0.9**	**83.8**
MS4-1	1070 [1765]	359	[355]	−0.27 [−0.4]	0.1 ± 0.4	18.1 ± 63.6
MS4-2	2975 [2975]		[357]	−0.28 [−0.3]		
Mean MS4				NS [NS]	NS	NS
MS5-1	720 [752]	389	[386]	−0.3 [−0.7]	*10.8 ± 3.2*	*−249.8 ± 58.2*
MS5-2	1425 [1460]		[386]	0.7 [0.3]	*66.1 ± 16.2*	*−290.3 ± 43.6*
MS5-3	2715 [2572]		[386]	3.2 [3.0]		
Mean MS5				NS [NS]	**34.2**	**−275.59**
MS6-1	790 [814]	362	[359]	−0.5 [−0.9]	*1.3 ± 0.5*	*−86.3 ± 39.4*
MS6-2	1385 [1409]		[359]	−0.9 [−1.2]	*−0.8 ± 0.1*	*66.8 ± 21.8*
MS6-3	2685 [2709]		[359]	−0.9 [−1.0]		
Mean MS6				**NS [NS]**	**−0.1**	**18.7**
MS7-1	505 [540]	281	[359]	1.7 [0.4]	*1.0 ± 0.4*	*−77.1 ± 26.6*
MS7-2	1195 [1224]		[359]	−1.2 [−0.5]	*2.3 ± 0.8*	*−64.9 ± 15.8*
MS7-3	2495 [2524]		[279]	−1.0 [−0.4]		
Mean MS7				NS [NS]	**1.5**	**−69.1**

[a]Temperature fluxes due to the mean flow are estimated in shear coordinate system, while eddy heat fluxes were estimated in 90d-LP coordinate system. Eddy heat fluxes estimated by *Nowlin et al.* [1985] are in brackets. Significant fluxes at a 95 % confidence level are in italic. Depth-averaged heat fluxes for each mooring are in bold.

Following *Sekma et al.* [2013], vertically integrated values of eddy heat flux are estimated using a layer thickness-weighted trapezoidal rule, setting statistically nonsignificant flux values to zero (Tables 2, and 3, Figure 8a). Eleven out of 24 values are significant and they all are negative, indicative of a poleward eddy heat flux, the largest value being 13.6 kW m^{-2}.

3.4. Model Eddy Heat Fluxes

Model eddy heat fluxes were computed at each level on the vertical at grid point as described above for the in situ data. A significance test was made and vertically integrated eddy heat fluxes over the same depths as the mooring data were estimated by setting nonsignificant flux values to zero (Figure 8a, values in parentheses). Model depth-integrated eddy heat fluxes vary between -31.3 and -1.2 kW m^{-2}, are negative or nonsignificant at the mooring locations and show similar order of magnitude to the in situ estimates. Large values are observed over the junction of the PAR and SFZ in the region of the SAF both in the model and the data (*Nowlin et al*., 1985), however, the values observed over the WSR in the PF region are larger in the in situ data (M4, M5, M6) than in the model outputs.

A complete map of depth-integrated model eddy heat fluxes reveals a patchy structure with mostly negative values, with spatial scales varying between 100 and 500 km (Figure 8b). Some spots of positive eddy heat fluxes are found in the center of the Yaghan Basin in the recirculation region. The depth-integrated model eddy fluxes range from -50 to 20 kW m^{-2}.

3.5. Model Eddy Heat Fluxes Integrated Over Mass-Balanced Regions

The model eddy heat fluxes integrated over the SAF, PF, and SACCF mass-balanced regions are all negative (poleward), with values of -0.03, -0.02, and -0.01 PW, respectively (Table 4). Values integrated over the areas between the SAF and PF mass-balanced regions or the PF and SACCF mass-balanced regions also provide negative mean eddy heat fluxes of -0.04 and -0.02 PW (Table 4). The mass-balanced region between the PF and the SAF shows the largest poleward mean eddy fluxes in spite of the positive eddy fluxes observed in the center of the Yaghan Basin (Figure 8b).

Therefore, in DP, the model provides reasonable eddy heat fluxes at the mooring location and shows an eddy heat flux that is maximum between the SAF and PF and then decreases southward. The order of magnitude of the poleward eddy heat flux in DP at 60°W is on the order of 2 % of the heat loss to the atmosphere south of 60°S, while the entire breadth of DP (between 48°W and 64°W) covers about 4% of the circumpolar longitudes and corresponds to a region of great eddy activity.

4. Across-Stream Heat Fluxes by the Time-Mean Flow

4.1. Method

Heat fluxes due to the mean flow across the ACC can be written as: $\oint \overline{LTF_{MF}}\,ds$, where the integration is taken along a circumpolar streamline s and $\overline{LTF_{MF}} = \rho_0 C_p \overline{V_p T} = 41.4\overline{V_p T}$ is the depth-integrated time-mean temperature flux at a given point. The heat flux across any vertical section can only make sense if the across-section volume flux is zero [*Montgomery*, 1974; *Hall and Bryden*, 1982]. Otherwise, the resulting flux value varies depending on the chosen unit of temperature (for example degree Kelvin rather than degree Celsius). The transport stream function shown in Figure 6 represents such a section, across which the volume flux is zero, by definition. Individual mean temperature fluxes are useful when considered as contribution to a whole mean heat flux if they are integrated along the transport stream function or over a mass-balanced region enclosed by nearby streamlines. This can only be done using outputs of a high-resolution numerical model because mooring data are sparse and distributed generally across (rather than along) the streamlines. Our strategy for using individual estimates from moorings is to validate the model-derived fluxes before they are integrated along the streamlines.

As our study is restricted to the Drake Passage, we computed model transport streamlines in the Drake Passage considering the Antarctic continent as a zero streamline (Figure 6), as already mentioned. To compute meridional heat fluxes, we integrated model individual mean temperature fluxes in mass-balanced regions (i.e., the areas between pairs of streamlines shown in Figure 6), which will be discussed in subsection 4.4. Estimation of across-stream temperature flux by the time-mean flow at a given point was made using a shear-coordinate system following *Sekma et al*. [2013]. Across-stream velocity time series $V_p(t)$ were calculated as the velocity component perpendicular to the daily direction of the vertical current shear between adjacent levels. Recall that in the shear coordinate system, the along-stream direction coincides with the direction of the thermal wind while the across-stream flow is perpendicular to isotherms such that the poleward (equatorward) temperature flux is associated with warm (cold) advection. The counterclockwise (clockwise) turning of the velocity vectors with decreasing depth is associated with warm (cold) advection, and no thermal advection occurs when the currents at both levels are parallel. A rotation of the velocity vector

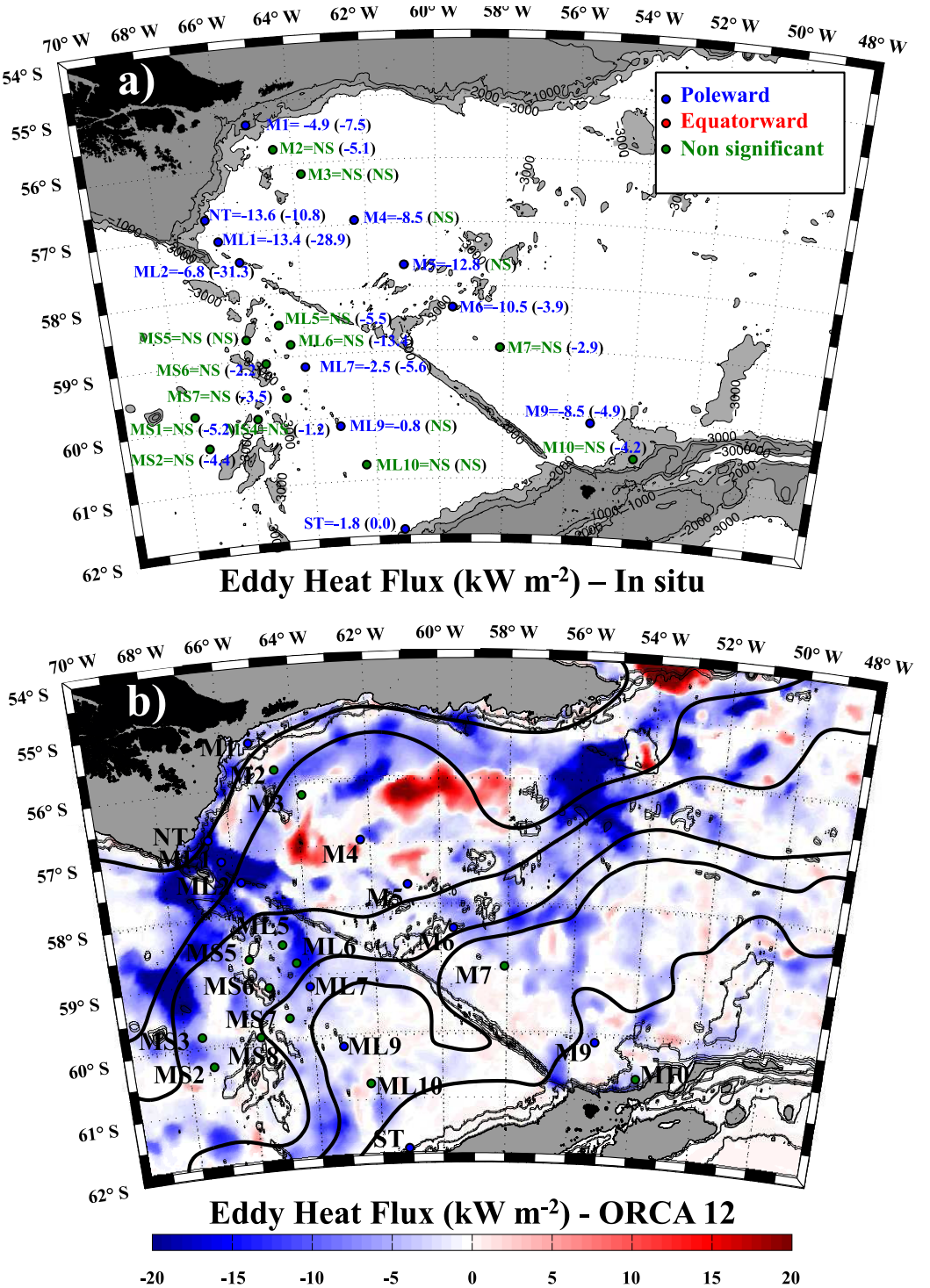

Figure 8. (a) Depth-averaged eddy heat flux values (in kW m^{-2}) estimated from current meter data using 90d-LP method. Poleward, equatorward, and nonsignificant heat fluxes are shown in blue, red, and green, respectively. All significant eddy fluxes are poleward with amplitudes smaller than 14 kW m^{-2}. Blue, red, and green dots at the mooring sites indicate, respectively, poleward, equatorward, and nonsignificant heat fluxes. Model eddy heat fluxes over the same depths as the mooring data are shown in parentheses. Isobaths (1000, 2000, and 3000 m) are plotted. Bottom topography shallower than 3000 m is shaded in gray. (b) Model eddy heat fluxes integrated from the bottom to surface. The model streamlines (see Figure 6) limiting the mass-balanced regions (SAF, PF, and SACCF regions) over which eddy heat fluxes are summed are shown in black solid lines. Blue, red, and green dots at the mooring sites indicate, respectively, poleward, equatorward, and nonsignificant heat fluxes as in Figure 8a).

Table 4. Estimates of Heat Flux (PW) Integrated Over Mass-Balanced Regions Defined by the Model Transport Streamlines: (a) Eddy Heat Flux, (b) Heat Flux Due to the Mean Flow, Values in Parentheses Correspond to the Ratio of the Heat Flux Due to Mean Flow Over the Eddy Heat Flux

Mass-Balanced Region	Surface/500 m	500 m/Bottom	0 m/Bottom
Eddy Heat Flux			
SAF	−0.008	−0.024	−0.031
SAF-PF	−0.007	−0.034	−0.041
PF	−0.007	−0.019	−0.026
SACCF - PF	−0.005	−0.014	−0.019
SACCF	−0.002	−0.008	−0.010
Heat Flux Due to the Mean Flow			
SAF	−0.017	−0.249	−0.266
	(2.1)	(10.4)	(8.6)
SAF-PF	−0.033	−0.274	−0.307
	(4.7)	(8.1)	(7.5)
PF	−0.010	−0.074	−0.085
	(1.4)	(3.9)	(3.3)
SACCF - PF	−0.005	−0.039	−0.044
	(1)	(2.8)	(2.3)
SACCF	−0.006	−0.039	−0.045
	(3)	(4.9)	(4.5)

suggests an upwelling or downwelling depending on the sense of the rotation [*Bryden*, 1976; *Schott and Stommel*, 1978]: a clockwise rotation for downwelling, and a counterclockwise rotation for upwelling in the Southern Hemisphere [*Sekma et al*., 2013]. Hence, a warm (cold) across-stream temperature flux is associated with upwelling (downwelling) in the ACC [*Phillips and Rintoul*, 2000; *Sekma et al*., 2013].

Combining the heat balance equation with the thermal wind equations and assuming small mixing, the vertical velocity w can be written as:

$$w=\frac{-\frac{\partial T}{\partial t}-\left(u\frac{\partial T}{\partial x}+v\frac{\partial T}{\partial y}\right)}{\frac{\partial \theta}{\partial z}}=\frac{-\frac{\partial T}{\partial t}-\frac{\rho_0 f}{g\alpha_e}\left(u\frac{\partial v}{\partial z}-v\frac{\partial u}{\partial z}\right)}{\frac{\partial \theta}{\partial z}} \tag{3}$$

where, T is in situ temperature, θ is the potential temperature (referenced to the sea surface), and α_e is the effective thermal expansion coefficient [e.g., *Bryden* 1976; *Lindstrom and Watts* 1994; *Phillips and Rintoul* 2000; *Sekma et al*., 2013].

The local mean temperature flux due to the time-mean flow $\overline{LTF}_{MF}$ is obtained by using:

$$\overline{LTF}_{MF}=\rho_0 C_P \overline{V_P T}=41.4\overline{V_P T}\ \ [\mathrm{kW\ m^{-2}}], \tag{4}$$

where the overbar denotes the record-length mean, $\rho_0 = 1035$ kg m^{-3}, $C_P \approx 4000$ J kg^{-1}°C^{-1} is the specific heat at constant pressure, and has been calculated in units of °C cm s^{-1} [e.g., *Nowlin et al*. 1985; *Phillips and Rintoul* 2000; *Sekma et al*., 2013]. The corresponding layer-mean temperature is obtained by averaging those from the upper and lower levels, such as $T(t)=\frac{[T_u(t)+T_l(t)]}{2}$. The time-mean total heat flux is determined by the product of the mean velocity $\overline{V}_P$ and the mean temperature $\overline{T}$, as $\overline{V_P T} \approx \overline{V}_P\,\overline{T}$ since $\overline{V'T'}$ was at least one order of magnitude smaller than $\overline{V}_P\,\overline{T}$ [*Sekma et al*., 2013]. The statistical significance of the mean at a 95% confidence level is tested following *Sekma et al*. [2013] by comparing with its standard error $SE=SD/\sqrt{N^*}$ multiplied by 2 where SD is the standard deviation of $V_P T$ about its mean and N^* the effective degrees of freedom, that is the length of the time series divided by the integral time scale τ defined as

$$\tau=\sum_{j=-M}^{M} C^2(j\Delta t)^2\Delta t \tag{5}$$

where C is the autocorrelation function of $V_P T$ and M equal to 20% of the number of observations [*Nowlin et al*., 1985].

4.2. Estimation of Vertical Velocities at the Moorings

The times series of cross-stream velocity V_P and vertical velocity w at midpoint levels are highly variable on different time scales (e.g., M4 in Figure 9). However, there appears clear evidence of a mean downwelling (negative w) at a number of levels (Table 2, column 6). During the first period (2006–2008) of DRAKE 2006–2009, the cross-stream velocity is predominantly positive (or northward), except for the 220 db layer at M1 and for the near bottom layers at M5 (not shown). The strongest and most systematic downwelling is observed in the near-bottom layer at M1 (620 db) and M4 (1075 db), with a significant time mean velocity of −50.97 m day^{-1} and −51.84 m day^{-1}, respectively. Another important downwelling throughout the entire water column is observed at M3, M6, and M9, with vertical velocities ranging from −6.91 to −33.69 m day^{-1}

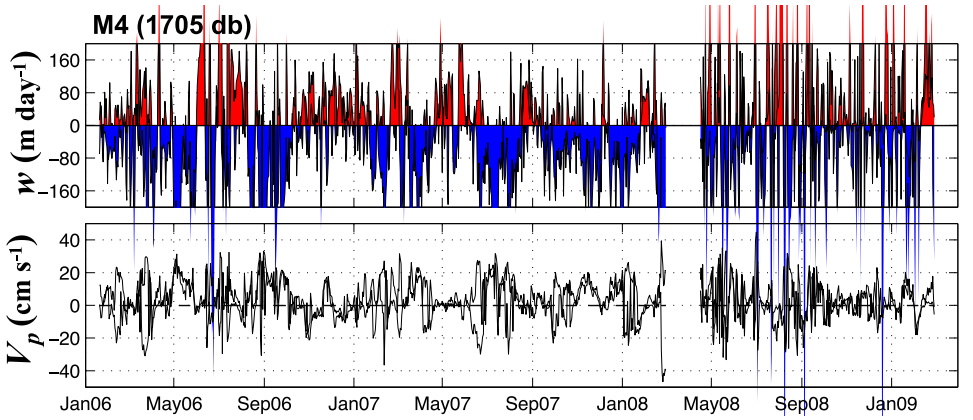

Figure 9. Typical examples of time series of the vertical velocity w and the cross-stream velocity V_p perpendicular to the thermal wind in shear coordinates at M4. Positive vertical velocities w (m day^{-1}) are shaded in red, and negative vertical velocities in blue. Time series of V_p (cm s^{-1}) are shown in green (thin line).

(Table 2, column 6). The strongest upwelling is obtained in the near-surface layers at M1 (220 db), with a significant time-mean velocity of 50.97 m day^{-1}. The weakest vertical motions are found at M7 with a weak downwelling (-0.87 m day^{-1}) at 720 db. The other time-mean vertical velocities are all negative except for 1865 db at M5, but they are not significant at a 95% confidence level. The two periods (2006–2008 and 2008–2009) of DRAKE 2006–2009 provide consistent values (when available). The significant time means of across-stream and vertical velocities give evidence of a prevailing cold advection associated to a downwelling over the entire water column at most of the mooring sites, except at the upper layers of the northernmost mooring at M1 over the continental shelf.

Vertical velocity time series (not shown) and their time means (Table 3, column 5) were also computed from the DRAKE 1979 data. Mean vertical velocities have similar amplitude to those estimated from the DRAKE 2006–2009 data set. However, in contrast to the DRAKE 2006–2009 estimates, significant positive vertical velocities, indicative of strong upwelling throughout the water column, are found for example at ML2 and MS5 (about 30 m day^{-1}) from the DRAKE 1979 data. This means that the sense of vertical motions is not homogeneous in DP but can change significantly in a relatively short spatial scale in either side of the SFZ. We will come back to this point in section 4.4.

4.3. Temperature Fluxes Due to the Time-Mean Flow at the Moorings

The resulting temperature fluxes due to the time-mean flow ($\overline{LTF}_{MF}$) are shown in the last column of Table 2. During the first period (2006–2008), most estimates of temperature fluxes due to the time-mean flow are significantly different from zero at a 95% confidence level. Only one third of the estimates are nonsignificant: M5, M7, and the upper levels of M4. The statistically significant fluxes correspond to a depth-mean northward temperature flux ranging from 101.4 ± 12.0 to 989 ± 141.9 kW m^{-2}, with the exception of M1 with a southward temperature flux of -1999.0 ± 386.6 kW m^{-2}. We estimated the depth-averaged temperature flux due to the time-mean flow separately for each mooring, using a layer thickness-weighted trapezoidal rule, setting statistically not significant flux values to zero. Aside from M1, estimated values are positive ranging from 101.4 ± 12.0 to 989 ± 141.9 kW m^{-2} for 2006–2008 and in general are consistent with those for 2008–2009 (Table 2). Estimates at M1 vary considerably between the two periods with a period-mean value of -70.8 ± 228.7 kW m^{-2} for 2006–2008 and $+74.3 \pm 216.7$ kW m^{-2} for 2008–2009. The average across-stream fluxes for all available instruments are 156.9 ± 111.1 kW m^{-2} for 2006–2008 and 107.6 ± 102.6 kW m^{-2} for 2008–2009, northward for both periods. These estimates represent a northward (equatorward) temperature flux caused by the time-mean flow. This equatorward temperature flux is consistent with the prevailing cold advection associated to the downwelling observed over the entire water column at most of the mooring sites, except at the upper layers of the northernmost mooring at M1 over the continental shelf (Figure 3).

Across-stream temperature fluxes by the mean flow from the DRAKE 1979 data were also estimated and are shown in the last column of Table 3. Half of the across-stream temperature fluxes (10 out of 24) are statistically significant. The largest amplitude of the temperature flux estimates are observed at ML2 (-711 kW m^{-2}) and

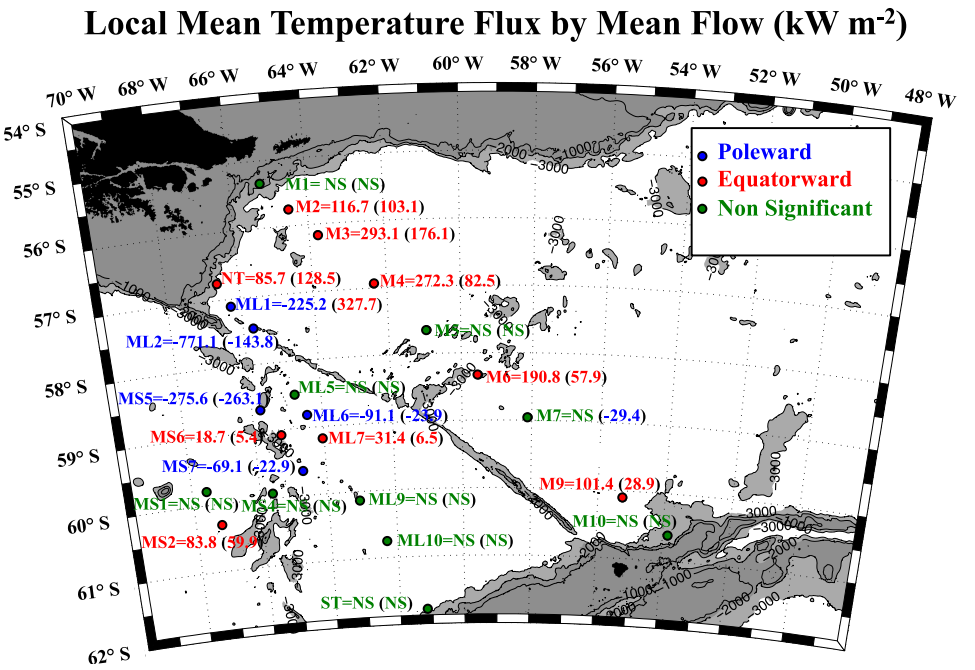

Figure 10. Depth-averaged cross-stream temperature flux (in kW m^{-2}) due to the time-mean flow estimated from current meter data. Poleward, equatorward, and nonsignificant temperature fluxes are shown in blue, red, and green, respectively. Model local mean temperature fluxes by mean flow over the same depths as the mooring data are shown in parentheses. Isobaths (1000, 2000, and 3000 m) are plotted. Bottom topography shallower than 3000 m is gray shaded.

MS5 (-275 kW m^{-2}). However, both equatorward and poleward significant cross-stream temperature fluxes by the mean flow are found. As expected, across-stream temperature fluxes due to the mean flow and mean vertical velocities are of opposite sign.

Depth-averaged temperature flux estimates caused by the mean flow are reported at each of the 24 mooring sites from both the DRAKE 1979 and DRAKE 2006–2009 (Figure 10): 10 estimates are non-significant, 9 are equatorward, and 5 are poleward. The spatial distribution of equatorward or poleward significant temperature fluxes caused by the mean flow is consistent with the local vertical velocity with an opposite sign.

4.4. Across-Stream Temperature Flux Caused by the Mean Flow in the Model Outputs

The temperature flux caused by the mean flow was computed from the model outputs, using the shear method applied to the 50 model levels. The statistical significance was computed as indicated in section 4.1. The depth-integrated temperature flux was computed, with statistically nonsignificant values set to zero. The model-derived depth-integrated temperature flux by the mean flow is heterogeneous and presents small spatial scales (Figure 11a). Amplitudes are larger in the north of DP than in the south. It is remarkable that the temperature flux caused by the mean flow in the model has the same sign as the estimates from in situ data at 11 out of the 14 mooring sites when those estimates are significant (Figure 10, model values in parentheses). The mooring site (ML1) where signs do not agree correspond to a location where model velocities poorly compare with in situ values. Spatial patterns of the mean temperature flux are clearly related to the bottom topography. An example is the structure of the depth integrated temperature flux caused by the mean flow over the narrow ridge of the SFZ with a change of sign at the top of the SFZ, with a negative (or poleward) heat flux just upstream the SFZ and a positive (or equatorward) heat flux downstream of the SFZ (Figure 11 a).

Model bottom vertical velocities (w) were estimated using $w=-\partial z_b(\frac{\partial u}{\partial x}+\frac{\partial v}{\partial y})_b$ where ∂z_b is the thickness of the bottom ocean level and $(\frac{\partial u}{\partial x}+\frac{\partial v}{\partial y})_b$ is the horizontal divergence of the flow at the bottom ocean level (vertical velocities were not stored as outputs). Time-mean bottom vertical velocities show small spatial scales with patterns reminiscent of that of the temperature flux caused by the mean flow with opposite sign (Figure 11b). Recall that bottom upwelling should be associated with a negative (or poleward) temperature flux and bottom downwelling with a positive (or equatorward) temperature flux. The consistency of

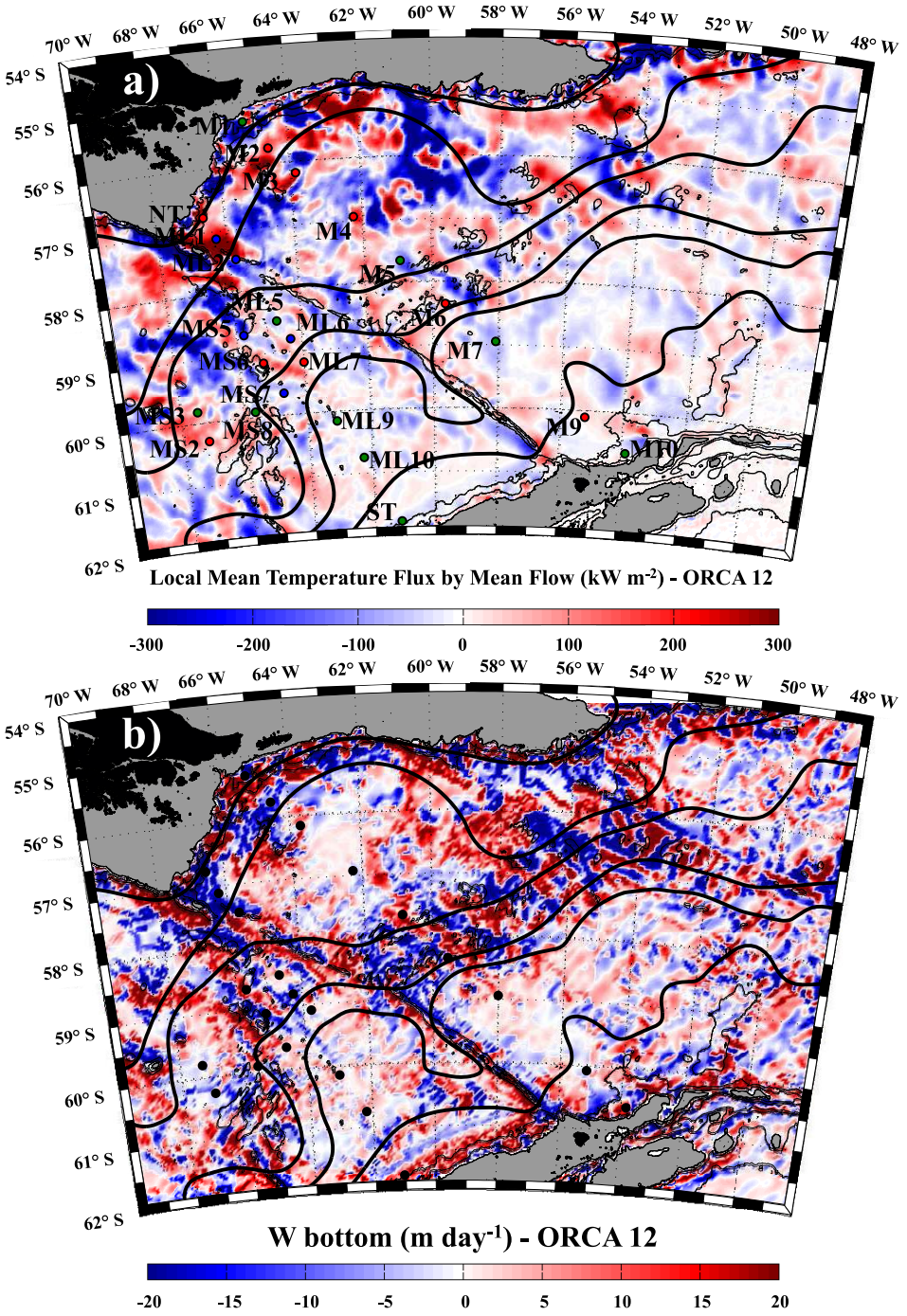

Figure 11. (a) Depth-averaged cross-stream temperature flux (in kW m^{-2}) due to the time-mean flow from Orca 12 model outputs. Blue, red, and green dots at the mooring sites indicate, respectively, poleward, equatorward, and nonsignificant temperature fluxes as in Figure 10. The model streamlines limiting the mass-balanced regions over which temperature fluxes are summed to produce heat fluxes due to the mean flow are shown in black lines. (b) Bottom velocity (in m day^{-1}) estimated from Orca 12 model outputs. Black dots indicate mooring locations. Streamlines as in Figure 11a.

this opposite sign between the mean temperature flux and the mean bottom vertical velocity was checked to yield the sign consistency at more than 80% of the grid points.

Depth-integrated temperature fluxes over the upper 500m are small and there is hardly any difference between the temperature fluxes integrated over the whole water column or integrated between 500 m and the bottom. This is assuring as most moorings have current meters at depths greater than 500 m.

4.5. Heat Flux Due to the Mean Flow in Mass-Balanced Regions

The model-derived temperature fluxes caused by the mean flow compare reasonably well with those estimated from the mooring data (Figure 10a). They are integrated over mass-balanced regions to obtain across-ACC heat fluxes. The mean heat fluxes due to the mean flow over the five mass-balanced regions defined in Figure 6 are all negative (poleward), with a maximum flux of −0.31 PW through the mass-balanced region between the SAF and PF and a flux of 0.27 PW through the SAF mass-balanced region. The poleward flux decreases sharply southward: a smaller flux of −0.08 PW through the PF mass-balanced region and the smallest flux of −0.04 PW between the PF and the SACCF and at the SACCF (Table 4).

5. Summary and Discussion

The contributions of the eddy flow and mean flow to the across-stream heat fluxes in DP have been calculated using two in situ mooring data sets in DP and outputs of a high-resolution numerical model of the ocean circulation. The two in situ mooring data sets, the year-long historical DRAKE 1979 data and the 3 year-long recent DRAKE 2006–2009 data, span the entire DP from north to south and are located in each side of a major submarine ridge, the SFZ.

5.1. Contribution of the Eddy Flow

All eddy heat fluxes derived from in situ data, when significant, are negative corresponding to a poleward heat flux (Tables 2 and 3). They are larger in the upper layers, in general. In the near-surface layers in DP, which are not resolved by the mooring data, large poleward eddy heat fluxes of up to 290 kW m^{-2} have been estimated from XBT/ADCP observations at the PF and SACCF, exceeding deep moored estimates by an order of magnitude [*Lenn et al*., 2011]. The only near surface time series, M1 at 60 m, provides the largest poleward eddy heat flux estimates (70–90 kW m^{-2} for the period 2006–2008). In contrast, during the 2008–2009 period, the poleward eddy heat flux at the same place and level was insignificantly small (between 1 and 3 kW m^{-2}), implying that interannual variations are important. Depth-integrated eddy fluxes were estimated, without the surface layer except at M1, providing negative (poleward) values when significant (Figure 5). The distribution of eddy heat fluxes is quite different between the upstream and downstream areas of the SFZ, with larger eddy heat fluxes at the SAF upstream of the SFZ [*Nowlin et al*., 1985] but larger eddy heat fluxes at the PF downstream of the SFZ. The largest depth-integrated eddy heat flux is of −13.6 kW m^{-2} at the SAF and 12.8 kW m^{-2} at the PF.

Model eddy heat fluxes compared satisfactorily with estimates from in situ moorings, both in amplitude and direction. They were mostly poleward except for the central Yaghan Basin, in the cyclonic recirculation region. Model eddy heat fluxes are of the same sign and larger in the upper layer than below 500 m. This is in agreement with the observations at M1, the unique mooring sampling the upper layer and where the calculation from XBT and LADCP was made by *Lenn et al*. (2011). However, the contribution of the upper 500 m did not significantly change the distribution nor the amplitude of the vertically integrated eddy heat flux (Table 4). The model vertically integrated eddy heat fluxes exhibit scales compatible with the size of mesoscale eddy activity. To make a large-scale budget, we relied on the model estimates, which compare rather well with the in situ mooring data. The model eddy heat fluxes integrated over the SAF, SAF-PF, PF, PF-SACCF, and SACCF mass-balanced regions are all negative or poleward, with values of −0.03, −0.04, −0.02, −0.02, and −0.01 PW, respectively (Table 4). Therefore, the model provides reasonable eddy heat fluxes at the mooring locations, showing a maximum between the SAF and PF and then decreasing southward. The order of magnitude of the poleward eddy heat flux in DP at 60°W is in the order of 2 % of the heat loss to the atmosphere south of 60°S, whereas DP (between 48°W and 64°W) covers about 4 % of the circumpolar longitudes and is a region of the ACC with a large EKE.

5.2. Cross-Stream Temperature and Heat Fluxes Due to the Mean Flow

Cross-stream temperature fluxes due to the mean flow show both positive and negative significant values at the mooring sites (Figure 10). Downstream of the SFZ, all the significant fluxes are positive, i.e., equatorward, in agreement with the general downwelling observed in the Yaghan and Ona Basins [*Ferrari et al*., 2012, 2013]. However, in the area upstream of the SFZ, the distribution of equatorward and poleward fluxes is more complex.

Model-derived temperature fluxes are of the same order of magnitude and when significant have the same sign as estimates from in situ observations with an 86% agreement (Figure 10). Model-derived depth-integrated temperature fluxes by the mean flow have values between +300 and −300 kW m^{-2} and exhibit small

spatial scales with alternating signs (Figure 11a). These small-scale patterns are similar to those of bottom vertical velocity estimates having opposite signs (Figures 11a and 11b). The bottom vertical velocity, estimated from the velocity nondivergence at the bottom, reflects the bottom slope with respect to the mean horizontal velocity. It has shown that the rotation of the mean velocity vectors with depth is mainly due to nonzero currents over sloping topography, in agreement with *Sekma et al*. [2013]. The rough hilly topography in DP leads to the small-scale vertical velocities and temperature fluxes. In contrast to the eddy heat flux, the contribution of the upper layer (0–500 m) is not significant for the heat flux due to the mean flow.

5.3. Respective Contributions of the Eddy and Mean Flows to the Poleward Heat Flux in DP

The integrated values along the mass-balanced regions delimited by different fronts in DP are all found to be poleward, with a maximum in the region between the SAF and PF for both eddy and mean flow contributions to the meridional heat flux. The contribution of the mean flow is larger than the eddy contribution for any of the mass-balanced regions, the ratio between the two varying between 8.6 (in the SAF region) and 2.3 (in the SACCF-PF region; Table 4). The model-estimated poleward heat flux across the SACCF in DP (covering about 4% of the circumpolar longitudes between 48°W and 64°W) is −0.055 PW (eddy contribution: −0.01, mean flow contribution −0.045 PW), i.e., in the order of 10% of the heat lost to the atmosphere south of 60°S. In other words, the across-stream heat flux in DP has a contribution from the mean flow of about 80% and the eddy flow for the remaining 20%. It plays a significant role for the circumpolar poleward heat flux despite its limited longitudinal extent.

The small spatial scales shown by the model-derived heat fluxes, for the mean flow contribution, and to a lesser extent for the eddy contribution, indicate that *Sekma et al*. [2013] circumpolar implications from a single point observation deserve confirmation. We are currently revisiting the other ACC mooring sites where in situ time series are available, e.g., south of Australia [*Phillips and Rintoul*, 2000], southeast of New Zealand [*Bryden and Heath*, 1985], computing heat fluxes due to the mean flow and comparing to model outputs in order to provide new circumpolar estimates in the near future. In parallel, within an international collaboration (Korea, France, USA), new mooring deployments are planned in the Udintsev Fracture Zone (57°S, 145°W) (Y.-H. Park and C. Provost, unpublished OSTST/CNES document, 2013), a major fracture zone in the path of the ACC where no in situ time series have ever been collected.

Acknowledgments

Financial support was provided both by the CNES (Centre National d'Etudes Spatiales) through the OSTST program and by CNRS–INSU (Institut des Sciences de l'Univers) through the LEFE program. R. Ferrari acknowledges an INEE (Institut National de l'Environnement et de l'Ecologie) Ph.D. scholarship and support from CNES after the Ph.D defense. The current meter data from DRAKE 2006–2009 are available at LOCEAN (cp@locean-ipsl.upmc.fr) and the velocity and temperature measurements from the DRAKE 1979 moorings are available at the Oregon State University buoy group database (http://cmdac.oce.orst.edu/). The ORCA 12 modelling experiment has been performed in the framework of the EU-funded MyOcean2 FP7 project. The model outputs from the ORCA 12 ocean model are available Mercator Océan (http://www.mercator-ocean.fr/) and the altimetry data at AVISO (www.aviso.altimetry.fr). The authors would like to thank the reviewers for their insightful comments and suggestions, which helped improve the manuscript.

References

Bernie, D. J, S. J. Woolnough, S. M. Slingo, and E. Guilyardi (2005), Modeling diurnal and intraseasonal variability of the ocean mixed layer, *J. Clim.*, *18*, 1190–1202, doi:10.1175/JCLI3319.1.

Bryden, H. L. (1976), Horizontal advection of temperature for low-frequency motions, *Deep Sea Res. Oceangr. Abstr.*, *23*, 1165–1174.

Bryden, H. L. (1979), Poleward heat flux and conversion of available potential energy in Drake Passage, *J. Mar. Res.*, *37*, 1–22.

Bryden, H. L., and R. A. Heath (1985), Energetic eddies at the northern edge of the Antarctic Circumpolar Current in the Southwest Pacific, *Prog. Oceanogr.*, *14*, 65–87.

Cronin, M., and D. R. Watts (1996), Eddy-mean flow interaction in the Gulf Stream at 68°W: Part I: Eddy energetics, *J. Phys. Oceanogr.*, *26*, 2107–2131.

Dee, D. P., et al. (2011), The era-interim reanalysis: Configuration and performance of the data assimilation system, *Q. J. R. Meteorol. Soc.*, *137*, 553–597, doi:10.1002/qj.828.

Ferrari, R., C. Provost, A. Renault, N. Sennéchael, N. Barré, Y.-H. Park, and J. H. Lee (2012), Circulation in Drake Passage revisited using new current time series and satellite altimetry: 1. The Yaghan Basin, *J. Geophys. Res.*, *117*, C12024, doi:10.1029/2012JC008264.

Ferrari, R., C. Provost, N. Barré, N. Sennéchael, and J. H. Lee (2013), Circulation in Drake Passage revisited using new current time series and satellite altimetry: 2. The Ona Basin, *J. Geophys. Res. Oceans*, *118*, 147–165, doi:10.1029/2012JC008193.

Fichefet, T., and M. A. M. Maqueda (1997), Sensitivity of a global sea ice model to the treatment of ice thermodynamics and dynamics, *J. Geophys. Res.*, *102*, 12,609–12,646, doi:10.1029/97JC00480.

Gordon, A. L., and W. B. Owens (1987), Polar oceans, *Rev. Geophys.*, *25*, 227–233.

Hall M. M., and H. L. Bryden (1982), Direct estimates and mechanisms of ocean heat transport, *Deep Sea. Res., Part A*, *29*, 339–359.

Hastenrath, S. (1982), On meridional heat transport in the world ocean, *J. Phys. Oceanogr.*, *12*, 922–927, doi:10.1175/1520-0485(1982)012<0922:OMHTIT>2.0.CO;2.

Hofmann, E. E., and T. Whitworth (1985), A synoptic description of the flow at Drake Passage from year-long measurements, *J. Geophys. Res.*, *90*, 7177–7187.

Killworth, P. D. (1992), An equivalent-barotropic mode in the fine resolution Antarctic model, *J. Phys. Oceanogr.*, *22*, 1379–1387.

Killworth, P. D., and C. W. Hughes (2002), The Antarctic Circumpolar Current as a free-equivalent-barotropic jet, *J. Mar. Res.*, *60*, 19–45.

Klinck, J. M. (1985), EOF analysis of Central Drake Passage Currents from DRAKE 79, *J. Phys. Oceanogr.*, *15*, 288–298, doi:10.1175/1520-0485(1985)015<0288:EAOCDP>2.0.CO;2.

Large, W. G., and S. G. Yeager (2009), The global climatology of an interannually varying air sea flux data set, *Clim. Dyn.*, *33*, 341–364, doi:10.1007/s00382-008-0441-3.

Lenn, Y.-D., T. K. Chereskin, J.S. Sprintall, and J. L. McClean (2011), Near-surface eddy heat and momentum fluxes in the Antarctic circumpolar current in drake passage, *J. Phys Oceanogr.*, *41*, 1385–1407, doi:10.1175/JPO-D-10-05017.1.

Lindstrom, S. S., and D. R. Watts (1994), Vertical motion in the Gulf Stream near 68°W, *J. Phys. Oceanogr.*, *24*, 2321–2333.

Madec, G. (2008), NEMO ocean engine, *Note du Pôle de Modélisation*, Report No. 27, NEMO ocean engine, Note du Pôle de Modélisation, Institut Pierre Simon Laplace (IPSL).

Meijers, A. J., N. L. Bindoff, and J. L. Roberts (2007), On the total, mean, and eddy heat and freshwater transports in the Southern Hemisphere of a 1/8° x 1/9° global ocean model, *J. Phys. Oceanogr.*, *37*, 277–295. doi:10.1175/JPO3012.1.

Montgomery R. B. (1974), Comments on "seasonal variability of the Florida Current" by Niiler and Richardson, *J. Mar. Res.*, *32*(3), 533–534.

Nowlin, W. D., Jr., S. J. Worley, and T. Whitworth III (1985), Methods for making point estimates of eddy heat flux as applied to the Antarctic Circumpolar Current, *J. Geophys. Res.*, *90*, 3305–3324.

Orsi, A. H., T. Whitworth, and W. D. Nowlin (1995), On the meridional extent and fronts of the Antarctic Circumpolar Current, *Deep Sea Res., Part I*, *42*, 641–673.

Park, Y.-H., and L. Gambéroni (1995), Large-scale circulation and its variability in the south Indian Ocean from TOPEX/Poseidon altimetry, *J. Geophys. Res.*, *100*, 24,911–24,929.

Phillips, H. E., and S. R. Rintoul (2000), Eddy variability and energetics from direct current measurements in the Antarctic Circumpolar Current south of Australia, *J. Phys. Oceanogr.*, *30*, 3050–3076.

Provost, C., A. Renault, N. Barré, N. Sennéchael, V. Garçon, J. Sudre, and O. Huhn (2011), Two repeat crossings of Drake Passage in austral summer 2006: Short-term variations and evidence for considerable ventilation of intermediate and deep waters, *Deep Sea Research Part II*, *58*, 25–26, pp. 2555–2572.

Rintoul, S. R., C. Hughes, and D. Olbers (2001), The Antarctic Circumpolar System, in *Ocean Circulation and Climate*, edited by G. Siedler, J. Church, and J. Gould, pp. 271–302, Academic Press, Oxford, U. K.

Schott, F., and H. Stommel (1978), Beta spirals and absolute velocities in different oceans, *Deep Sea Res.*, *25*(11), 961–1010.

Sekma, H., Y.-H. Park, and F. Vivier (2013), Time-mean flow as the prevailing contribution to the poleward heat flux across the southern flank of the Antarctic Circumpolar Current: A case study in the Fawn Trough, Kerguelen Plateau, *J. Phys. Oceanogr.*, *43*, 583–601.

Volkov, D. L., L.-L. Fu, and T. Lee (2010), Mechanisms of the meridional heat transport in the Southern Ocean, *Ocean Dyn.*, *60*, 791–801.

Walkden, G. J., K. J. Heywood, and D. P. Stevens (2008), Eddy heat fluxes from direct current measurements of the Antarctic Polar Front in Shag Rocks Passage, *Geophys. Res. Lett.*, *35*, L06602, doi:10.1029/2007GL032767.

Whitworth, T. III (1983), Monitoring the transport of the Antarctic Circumpolar Current at Drake Passage, *J. Phys. Oceanogr.*, *13*(11), 2045–2057.

Whitworth, T. III, D. Nowlin Jr., and J. Worley (1982), The net transport of the Antarctic Circumpolar Current through Drake Passage, *J. Phys. Oceanogr.*, *12*, 960–971.